Advancing high-temperature electrostatic energy storage *via* linker engineering of metal–organic frameworks in polymer nanocomposites

Zongliang Xie, ‡[abc] *Zhiyuan Huang,* ‡[b] *He Li,* ‡[ab] *Tianlei Xu,*[c] *Haoyu Zhao,*[d] *Yunfei Wang,*[de] *Xi Pang,*[c] *Zhiqiang Cao,*[d] *Virginia Altoé,*[b] *Liana M. Klivansky,*[b] *Zaiyu Wang,*[ef] *Steve W. Shelton,*[b] *Shiqi Lai,*[bg] *Peng Liu,*[c] *Chenhui Zhu,*[e] *Michael D. Connolly,*[b] *Corie Y. Ralston,*[b] *Xiaodan Gu,*[d] *Zongren Peng,*[c] *Jian Zhang* *[b] *and Yi Liu* *[ab]*

[a.] *Materials Sciences Division, Lawrence Berkeley National Laboratory, Berkeley, CA 94720, USA. E-mail: yliu@lbl.gov*

[b.] *The Molecular Foundry, Lawrence Berkeley National Laboratory, Berkeley, CA 94720, USA. E-mail: jianzhang@lbl.gov*

[c.] *State Key Laboratory of Electrical Insulation and Power Equipment, Xi'an Jiaotong University, Xi'an, Shaanxi 710049, P. R. China.*

[d.] *School of Polymer Science and Engineering, Center for Optoelectronic Materials and Devices, The University of Southern Mississippi, Hattiesburg, MS 39406, USA.*

[e.] *Advanced Light Source, Lawrence Berkeley National Laboratory, Berkeley, CA 94720, USA.*

[f.] *Department of Chemistry and the Hong Kong Branch of the Chinese National Engineering Research Center for Tissue Restoration and Reconstruction, The Hong Kong University of Science and Technology, Hong Kong 999077, P. R. China.*

[g.] *Department of Chemistry, University of California, Berkeley, CA 94720, USA.*

[†] *Electronic Supplementary Information (ESI available. See DOI: 10.1039/x0xx00000x*

[‡] *These authors contributed equally to this work.*

Table S1 Previously published works on high-temperature polymer/inorganic filler systems.

| Dielectric materials	150 °C		200 °C		Ref.
	Applied field $(MV\ m^{-1})$	U_d with $\eta>90\%$ $(J\ cm^{-3})$	Applied field $(MV\ m^{-1})$	U_d with $\eta>90\%$ $(J\ cm^{-3})$	
PEI/Al$_2$O$_3$	/	/	650	6.8	*Adv. Mater.*, 2023, **35**, 2301936.
PEI/ZrO$_2$@COF	600	6.2	/	/	*Adv. Funct. Mater.*, 2024, **34**, 2314910.
PEI/Al$_2$O$_3$@ZrO$_2$	450	3.8	/	/	*Adv. Energy Mater.*, 2021, **11**, 2101297.
F-PI-PWNS	810	8.0	740	7.2	*Nat. Energy*, 2024, **9**, 143.
PI-3.0	575	5.3	475	3.6	*Adv. Mater.*, 2023, **35**, 2211487.
c-BCB/BNNS	400	2.2	200	0.6	*Nature*, 2015, **523**, 576.
PI/Al$_2$O$_3$	300	1.6	/	/	*Adv. Energy Mater.*, 2020, **10**, 1903881.
PEI/SiO$_2$	600	6.3	/	/	*Small*, 2022, **18**, 2202421.
PEI/HAP	550	5.1	400	3.1	*Adv. Funct. Mater.*, 2023, **33**, 2214100
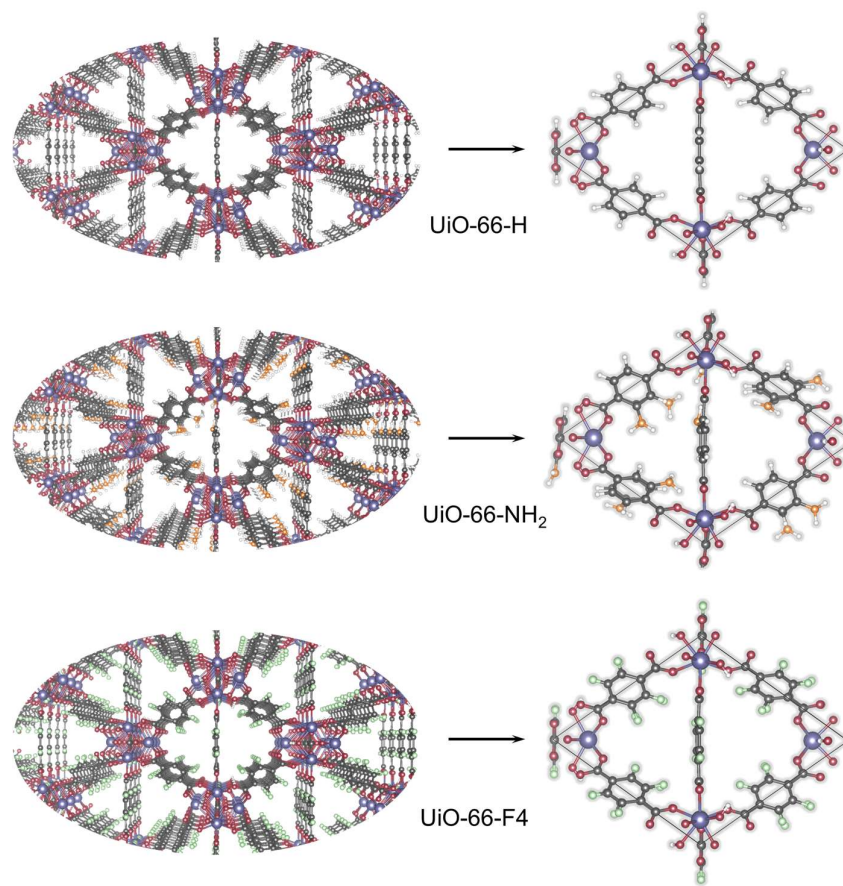
Fig. S1 DFT-optimized periodic framework structures (left) and primitive cells (right) of UiO-66-H, UiO-66-NH$_2$ and UiO-66-F4. Gray-colored atoms represent C, white-colored atoms represent H, red-colored atoms represent O, orange-colored atoms represent N, and purple-colored atoms represent F.
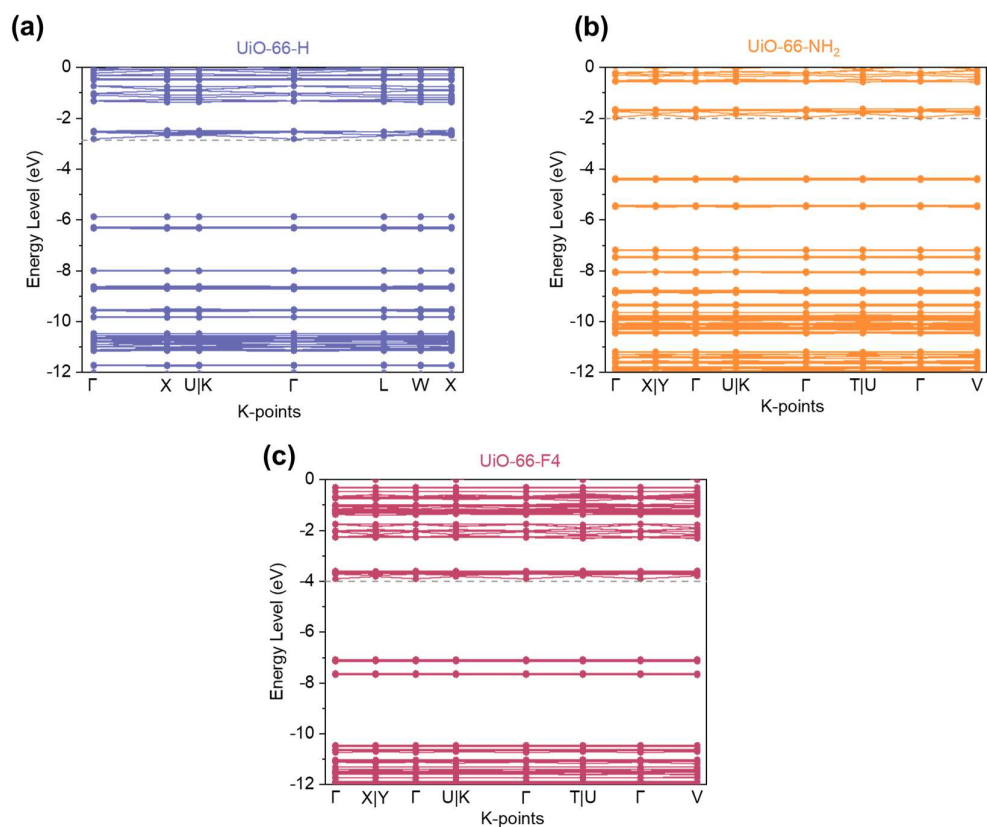
Fig. S2 Calculated band structures of (a) UiO-66-H, (b) UiO-66-NH$_2$ and (c) UiO-66-F4.
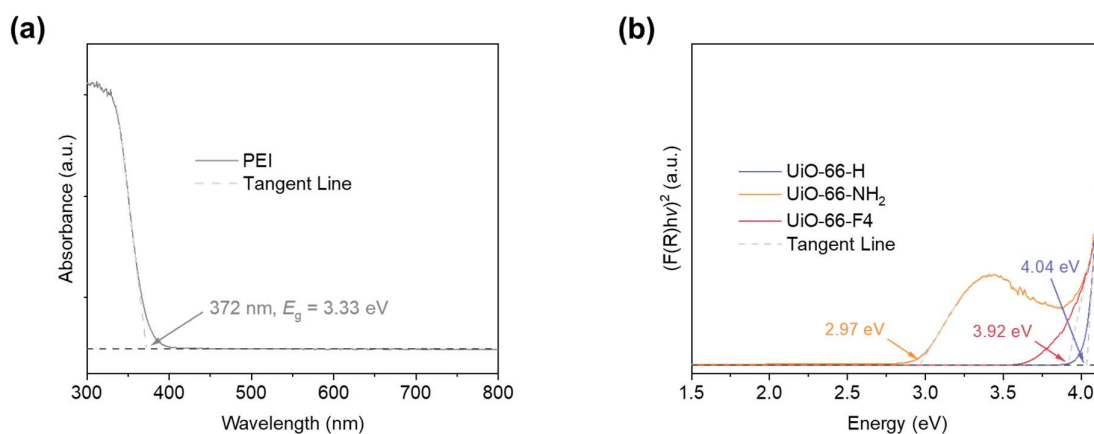
Fig. S3 (a) UV-vis absorption spectrum of PEI. **(b)** Tauc plots of MOFs based on their UV-vis diffuse reflectance spectra. The band gap of PEI was determined as 3.33 eV from the absorption onset of the linear region, while the band gaps for UiO-66-H, UiO-66-NH$_2$ and UiO-66-F4 were determined from the Tauc plots to be 4.04 eV, 3.92 eV and 2.97 eV, respectively.
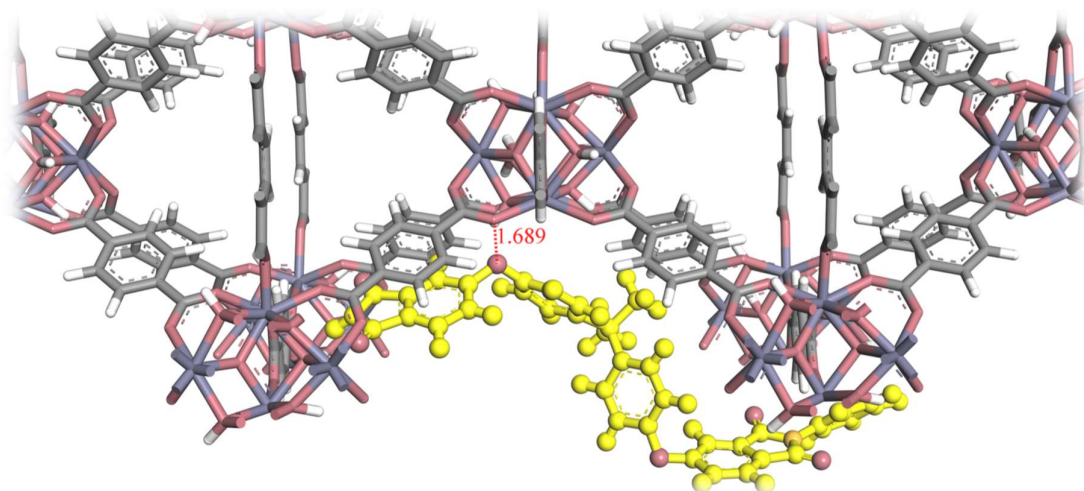
Fig. S4 Molecular structure of a segment of PEI and MOF UiO-66-H after molecular dynamics optimization. Gray-colored atoms represent C, white-colored atoms represent H, red-colored atoms represent O, orange-col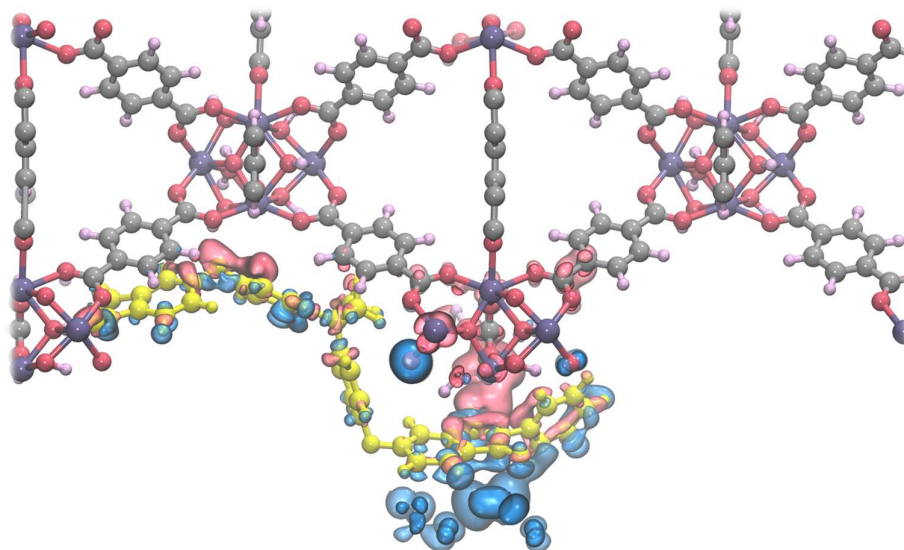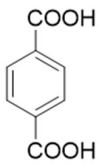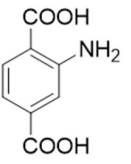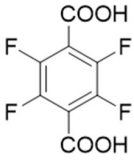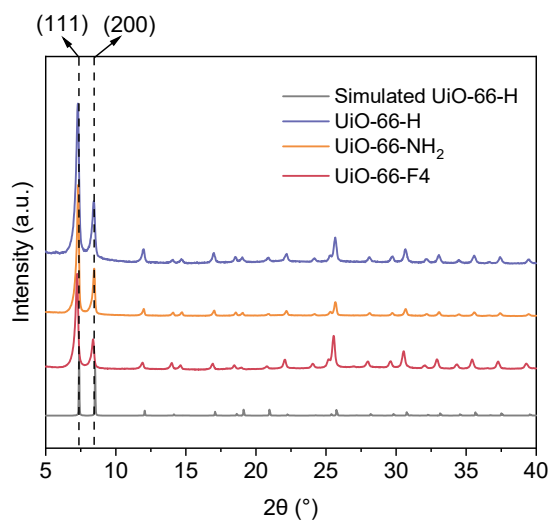ored atoms represent N, and purple-colored atoms represent Zr. PEI chain was highlighted in yellow. The short contact distance between the etheric oxygen atoms in PEI and the hydroxyl protons in the MOF clusters suggests favorable hydrogen bonding interactions.

Fig. S5 Charge density difference between MOF UiO-66-H and PEI. PEI chain was highlighted in yellow. Gray-colored atoms represent C, pink-colored atoms represent H, red-colored atoms represent O, orange-colored atoms represent N, and purple-colored atoms represent Zr. A significant charge density difference in the regions between the imide groups of PEI and the MOF clusters can be observed. The red areas represent electron-rich components with positive charge differences after intermolecular interactions; the blue areas represent electron-deficient groups with negative charge differences after intermolecular interactions.

Table S2 Synthetic conditions for MOF fillers.

Material	Ligand	Modulators (ration to ligand)	Solvent	Reaction conditions
UiO-66-H	COOH (benzene ring) COOH	Formic acid (70 eq.)	DMF (12 ml)	120 °C, 24 h
UiO-66-NH$_2$	COOH NH$_2$ (benzene ring) COOH	Benzoic acid/H$_2$O (30/4 eq.)	DMF (12 ml)	120 °C, 24 h
UiO-66-F4	COOH F F (benzene ring) F F COOH	HCl (10 eq.)	THF (12 ml)	90 °C, 24 h

Fig. S6 Powder X-ray diffraction (PXRD) patterns of UiO-66-H, UiO-66-NH$_2$, UiO-66-F4, and the simulated XRD pattern of UiO-66-H.
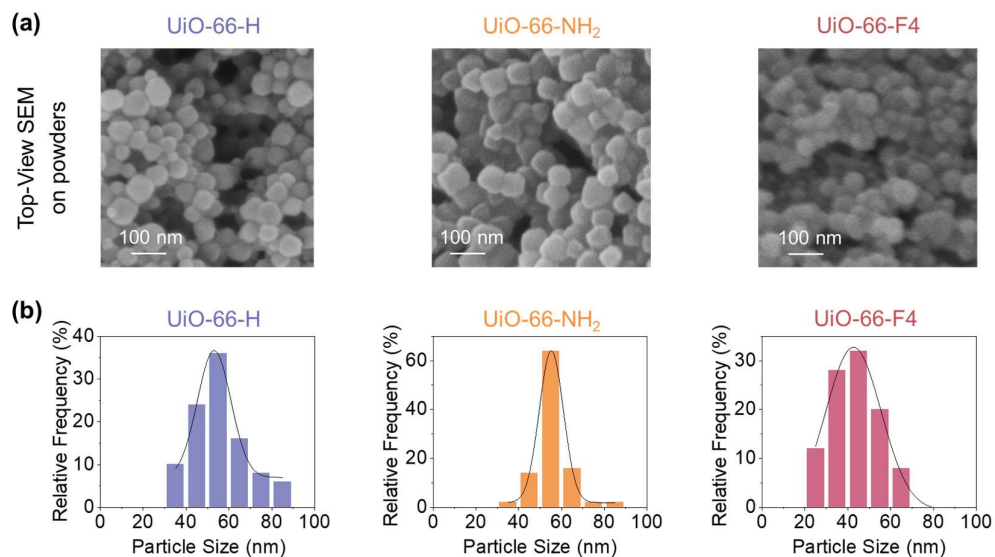
Fig. S7 (a) Scanning electron microscopy (SEM) images and (b) size distribution analysis of MOFs UiO-66-H, UiO-66-NH$_2$ and UiO-66-F4. The particle sizes of UiO-66-H, UiO-66-NH$_2$, and UiO-66-F4 were determined using ImageJ® software, with values of 53.1 ± 12.3 nm, 55.8 ± 8.0 nm and 43.3 ± 10.7 nm, respectively (presented as mean ± standard deviation).
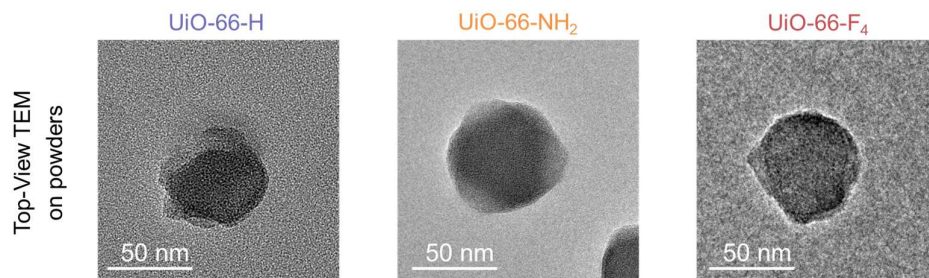
Fig. S8 Transmission electron microscope (TEM) images of UiO-66-H, UiO-66-NH$_2$ and UiO-66-F4.
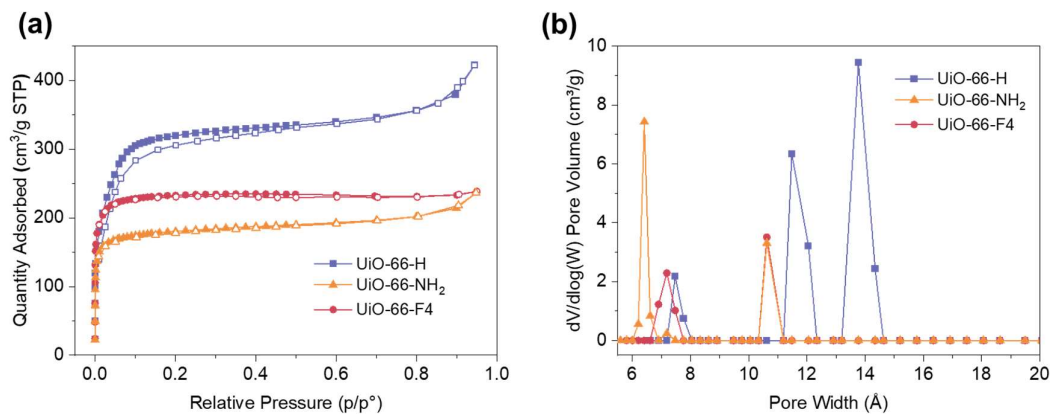
Fig. S9 (a) Nitrogen adsorption isotherms and (b) pore size distribution of UiO-66-H, UiO-66-NH$_2$ and UiO-66-F4.

Table S3 BET surface areas of UiO-66-H, UiO-66-NH$_2$ and UiO-66-F4.

Material	BET Surface Area (m^2 g^{-1})
UiO-66-H	1292
UiO-66-NH$_2$	708
UiO-66-F4	935
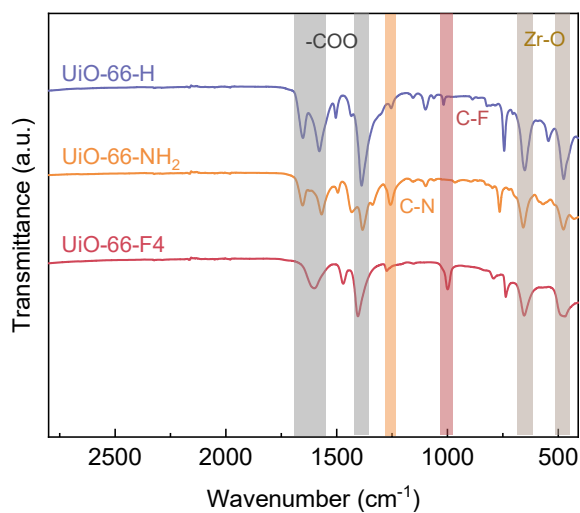
Fig. S10 FTIR spectra of UiO-66-H, UiO-66-NH$_2$ and UiO-66-F4.
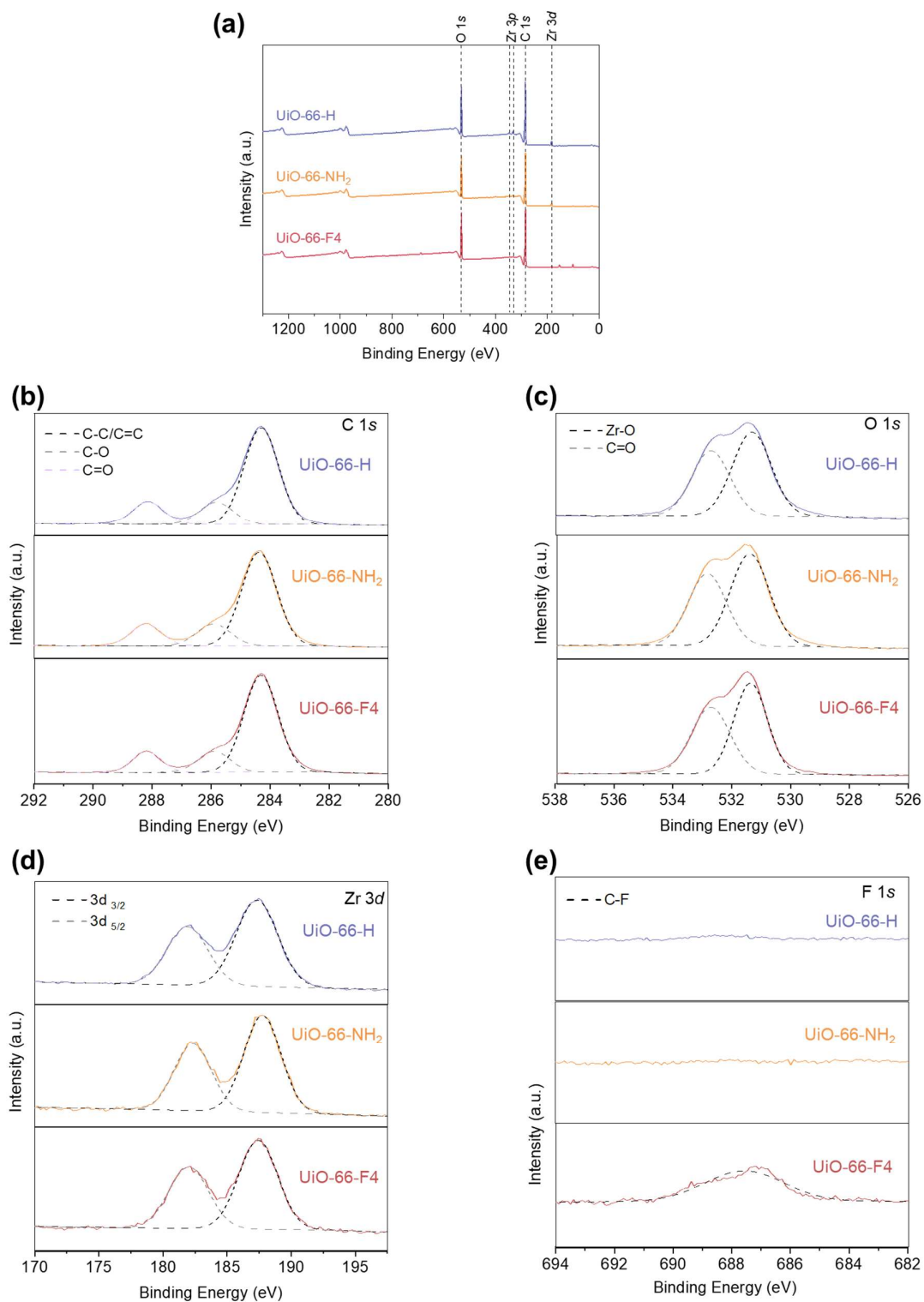
Fig. S11 (a) X-ray photoelectron spectroscopy (XPS) survey scans of UiO-66-H, UiO-66-NH$_2$ and UiO-66-F4. Peaks and fitting at binding energies for (b) C 1s, (c) O 1s, (d) Zr 3d and (e) F 1s.
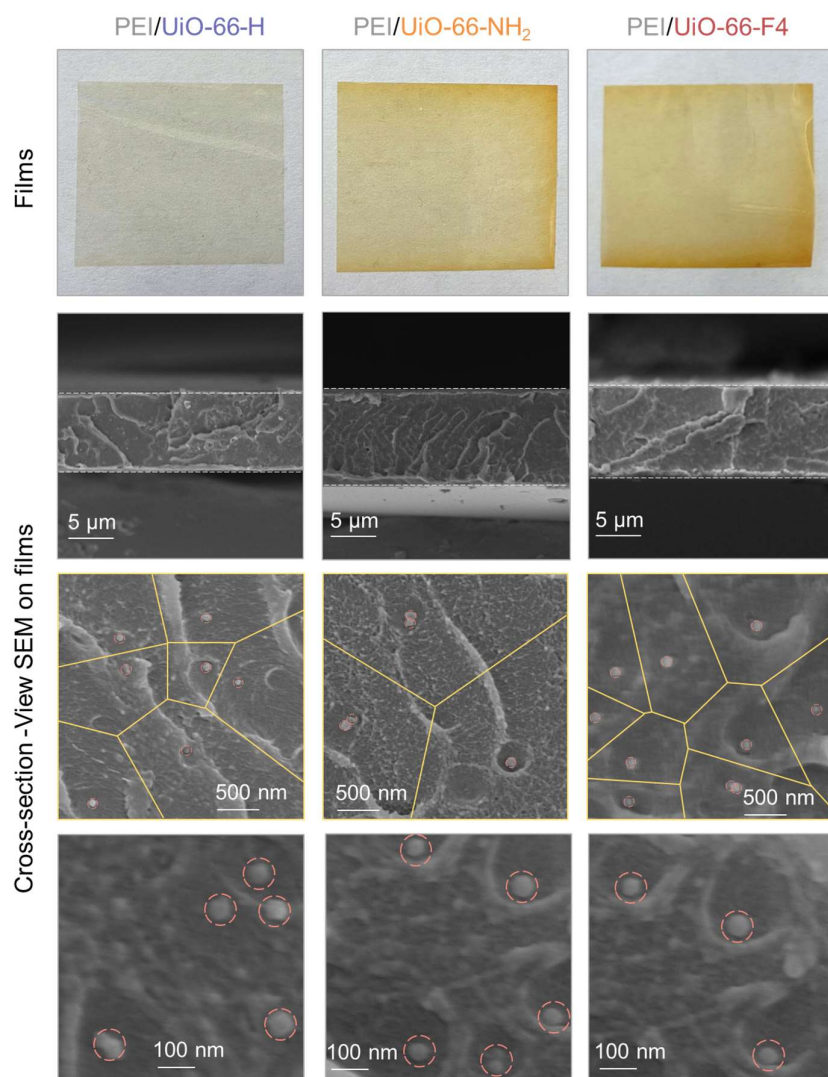
Fig. S12 Digital photos and cross-sectional SEM figures of PEI/UiO-66-H, PEI/UiO-66-NH$_2$ and PEI/UiO-66-F4 composite films at 1 wt% filler loading. MOFs are highlighted with red-dotted circles, and their distribution within the PEI matrix is evaluated using Voronoi diagrams (marked by yellow lines). The average diameter of the Voronoi polygons exceeds 500 nm, indicating a good dispersion of the MOFs within the PEI matrix.
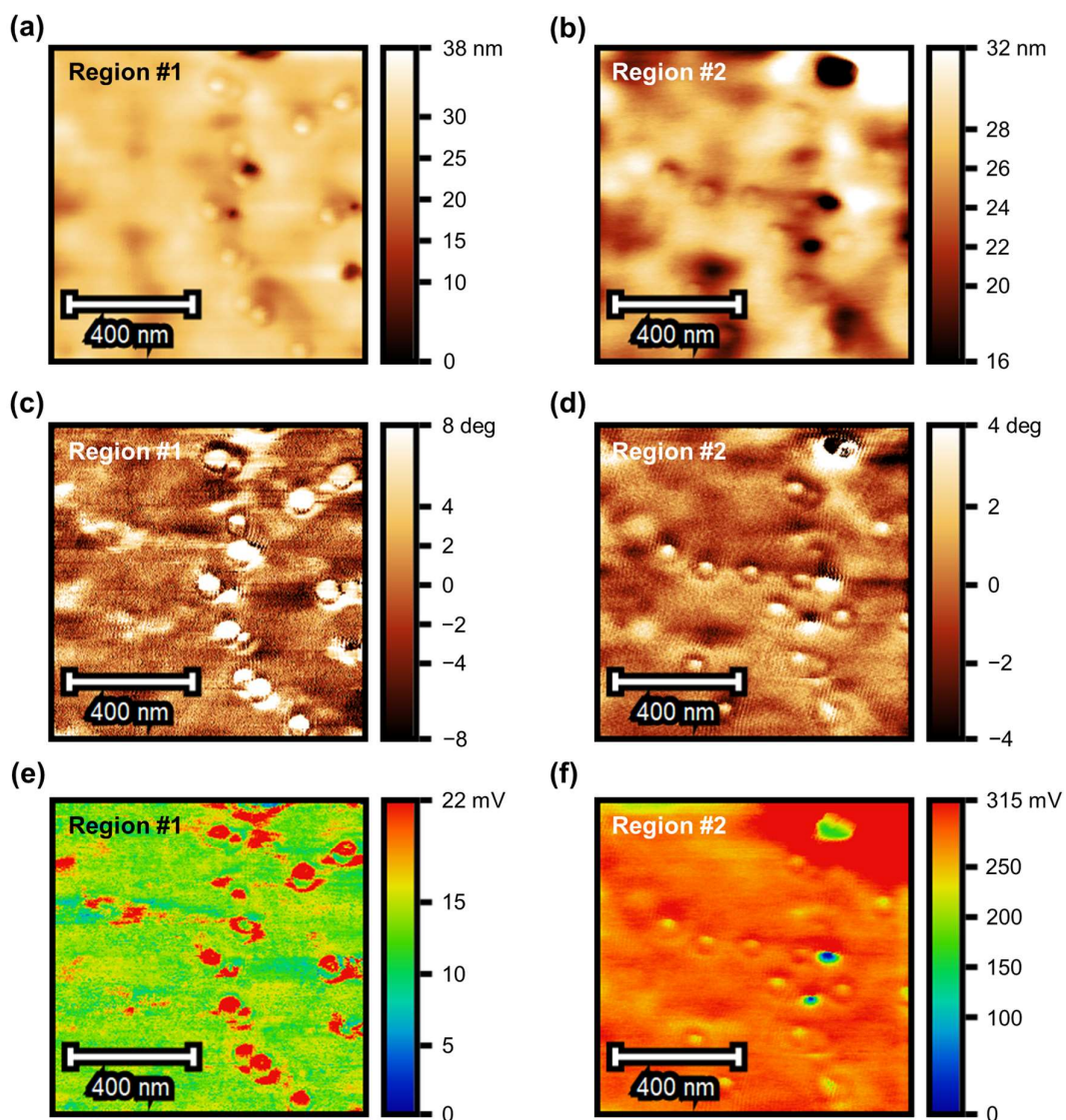
Fig. S13 Comprehensive AFM studies of the PEI/UiO-66-F4 composite film at 1 wt% filler loading at two different localized regions. (a) AFM height image, (c), AFM phase image and (e) AFM-IR mapping probed at the wavenumber of 1404 cm^{-1} (characteristic of MOF particle) at region #1. (b) AFM height image, (d) AFM phase image and (f) AFM-IR mapping probed at the wavenumber of 1718 cm^{-1} (characteristic of PEI) at region #2.
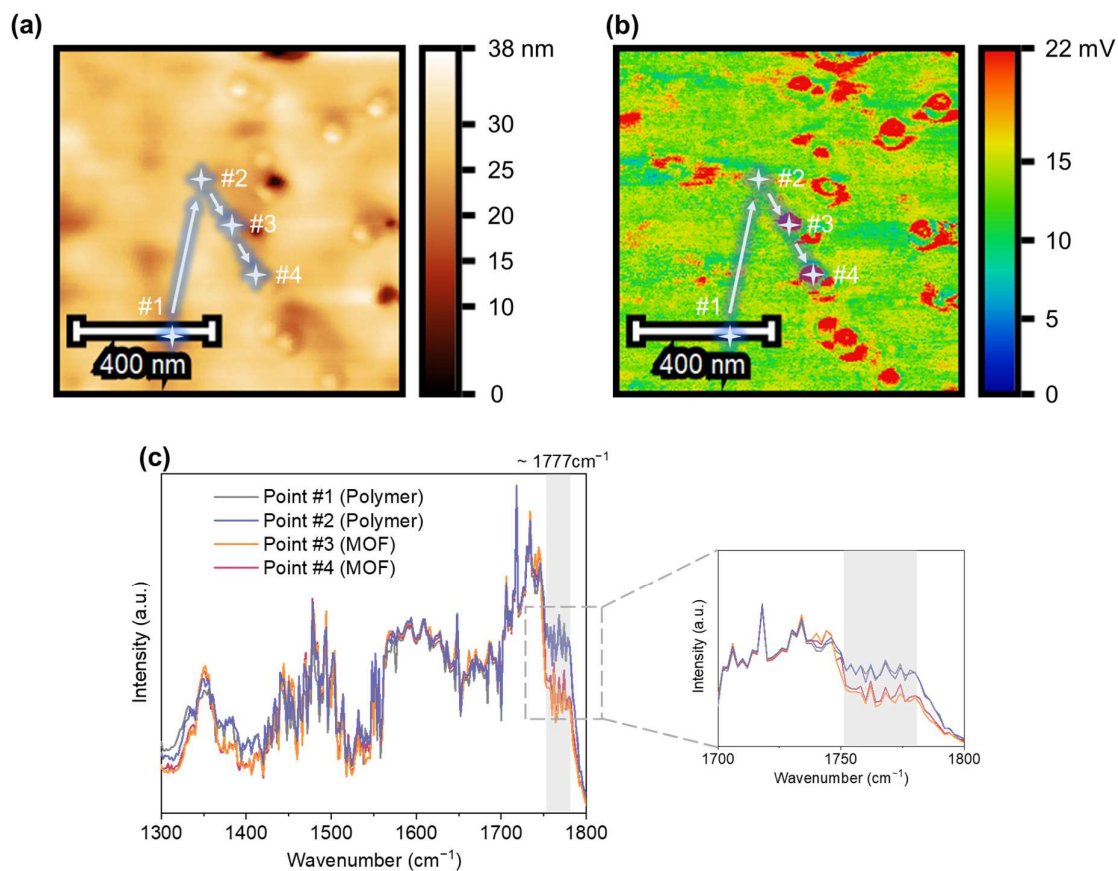
Fig. S14 Zone analysis of the PEI/UiO-66-F4 composite film (at 1 wt% filler loading) showing the dispersion of MOF particles in the polymer matrix. (a) AFM height image and (b) AFM-IR mapping probed at the wavenumber of 1404 cm^{-1}. The blue-colored crosses represent four individual locations, labeled as #1–#4. #1 and #2 are polymer-only regions while #3 and #4 are PEI-MOF interfacial regions. (c) IR spectra at the four locations in the wavenumber range of 1300–1800 cm^{-1}. The contrast highlighted in the shaded region in (c) reveals spectroscopic differences between regions of pure PEI and PEI/MOF composites.
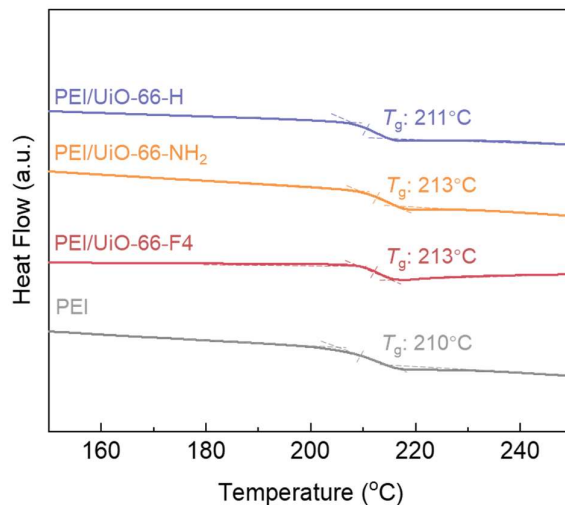
Fig. S15 Differential scanning calorimetry (DSC) curves showing the glass transition temperature (T_g) of PEI, PEI/UiO-66-H, PEI/UiO-66-NH$_2$ and PEI/UiO-66-F4 composite films at 1 wt% filler loading.
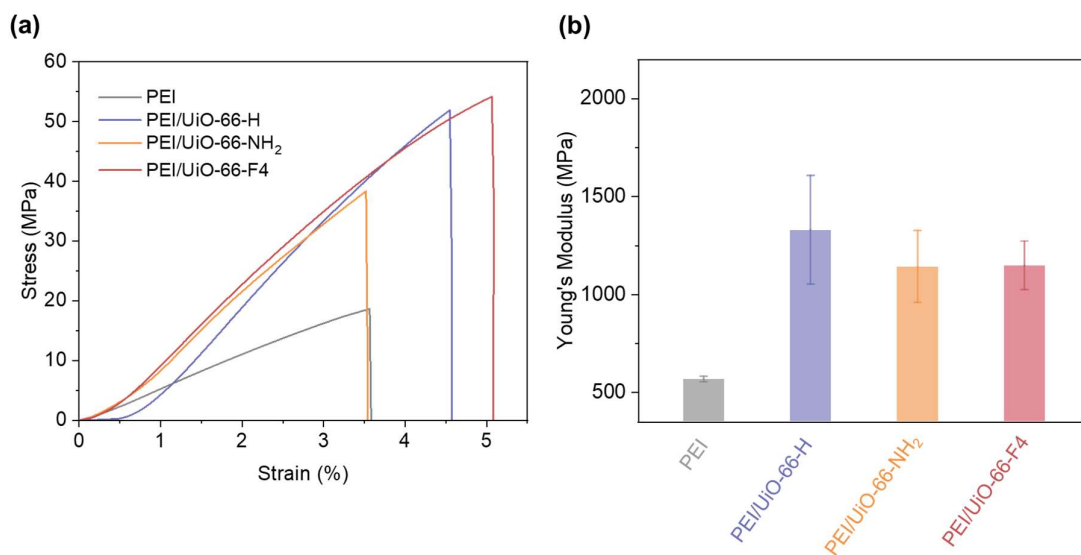
Fig. S16 (a) Strain–stress curves derived from tensile tests, and (b) comparison of Young's modulus among PEI, PEI/UiO-66-H, PEI/UiO-66-NH$_2$ and PEI/UiO-66-F4 composite films at 1 wt% filler loading, derived from dynamic mechanical analysis (DMA) tests.
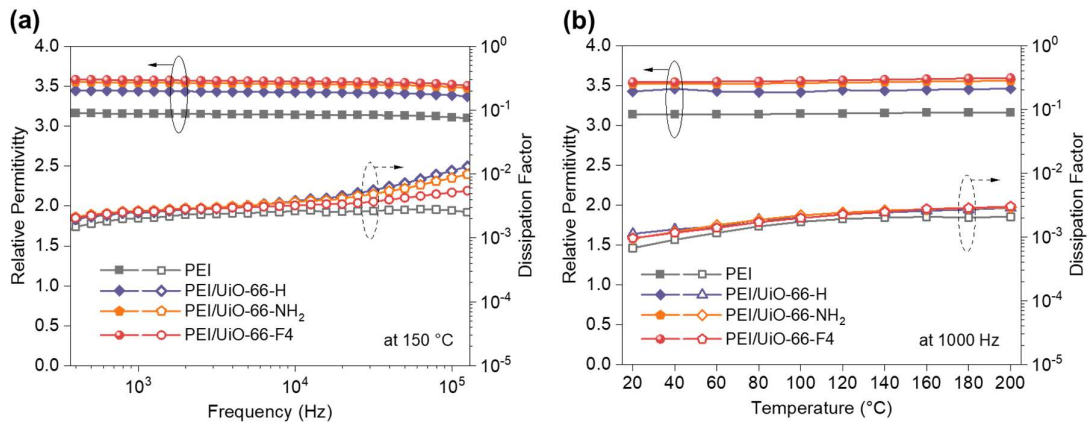
Fig. S17 (a) Frequency-dependent dielectric spectra at 150 °C. (b) Temperature-dependent dielectric spectra of PEI, PEI/UiO-66-H, PEI/UiO-66-NH₂ and PEI/UiO-66-F4 composite films at 1 wt% filler loading under 1000 Hz.
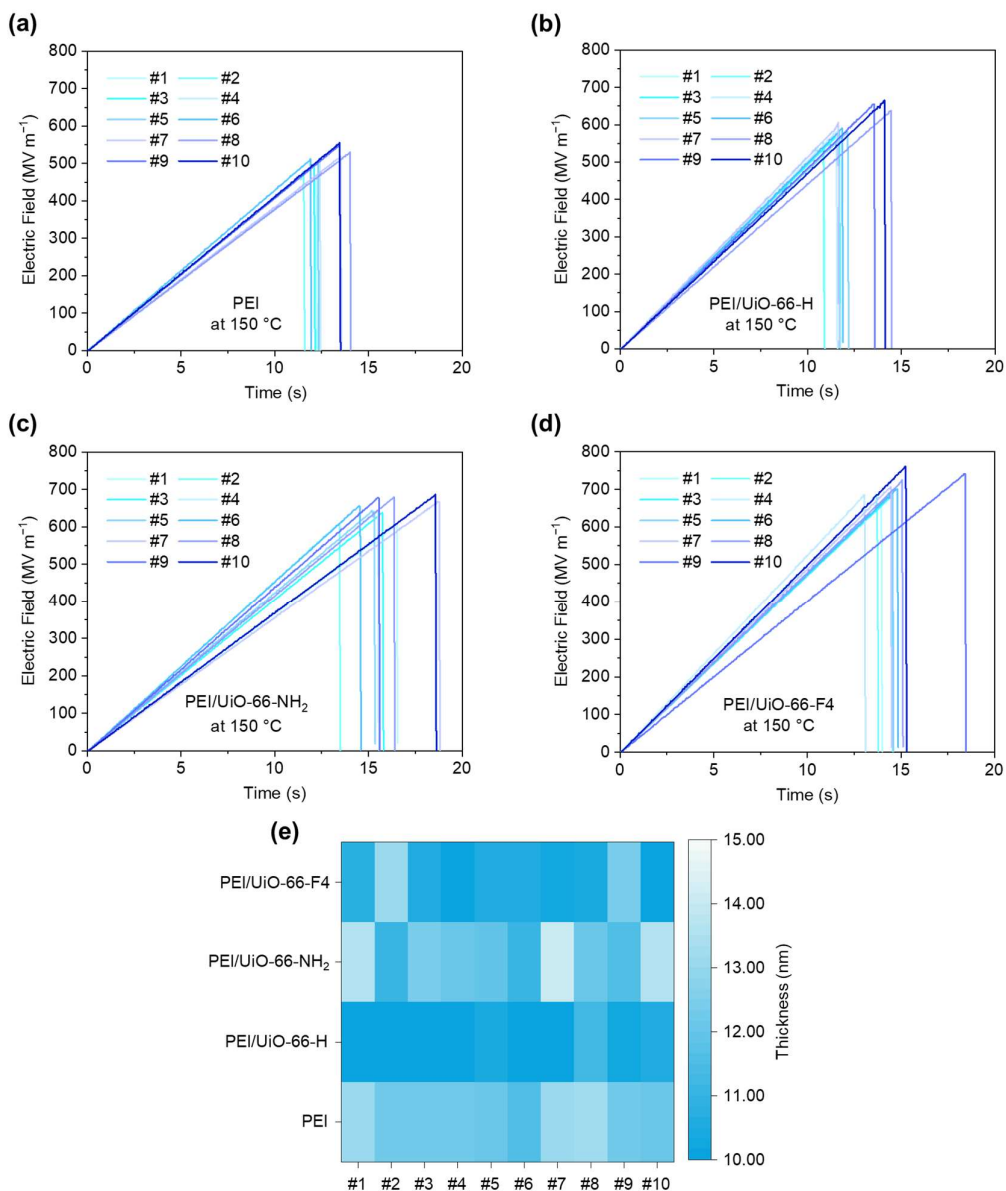
Fig. S18 Breakdown testing curves of (a) PEI, (b) PEI/UiO-66-H, (c) PEI/UiO-66-NH$_2$, and (d) PEI/UiO-66-F4 composite films at 1 wt% filler loading at 150 °C. (e) Thicknesses of all testing devices of PEI, PEI/UiO-66-H, PEI/UiO-66-NH$_2$ and PEI/UiO-66-F4 composite films.
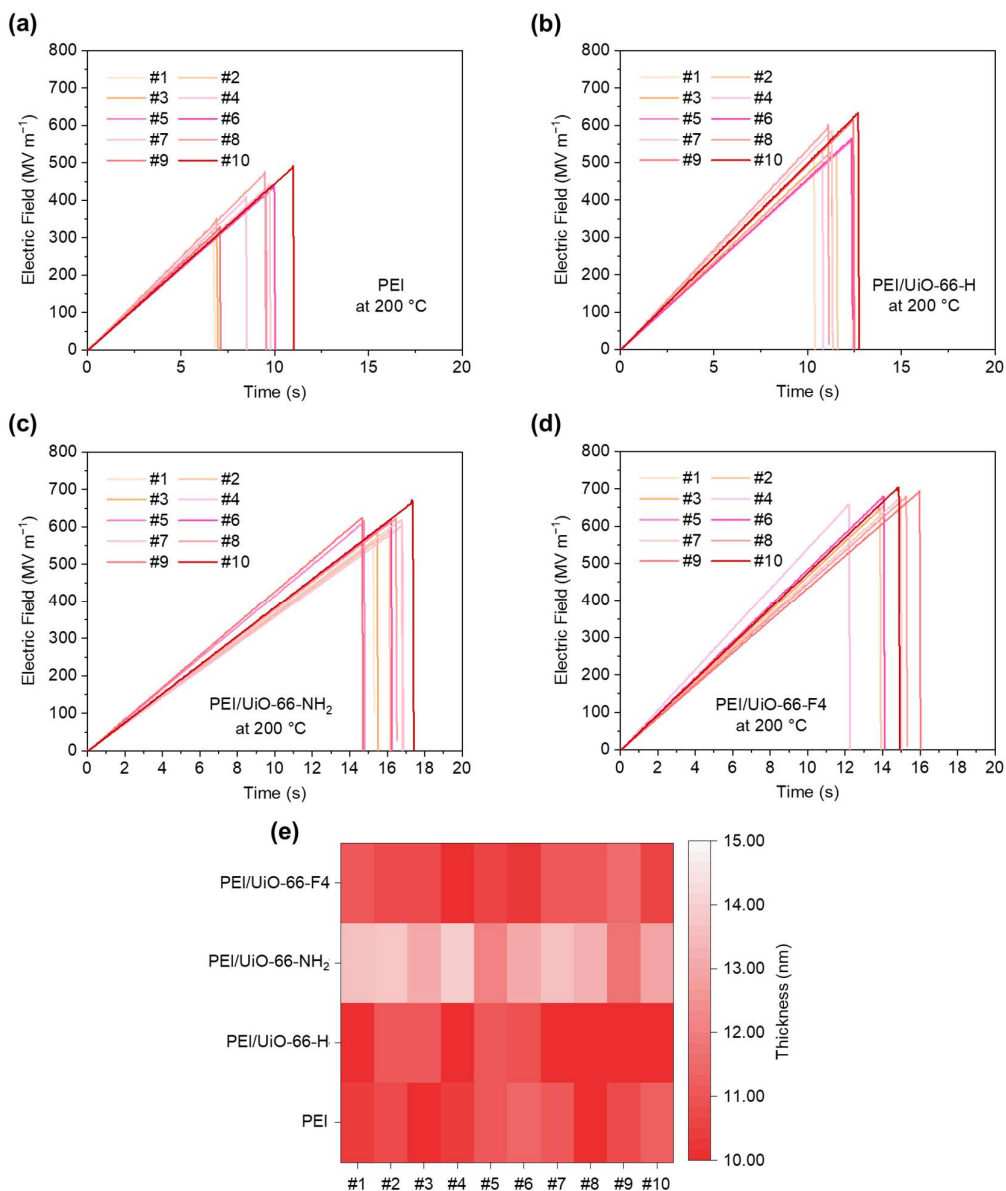
Fig. S19 Breakdown testing curves of (a) PEI, (b) PEI/UiO-66-H, (c) PEI/UiO-66-NH$_2$, and (d) PEI/UiO-66-F4 composite films at 1 wt% filler loading at 200 °C. (e) Thicknesses of all testing devices of PEI, PEI/UiO-66-H, PEI/UiO-66-NH$_2$ and PEI/UiO-66-F4 composite films.
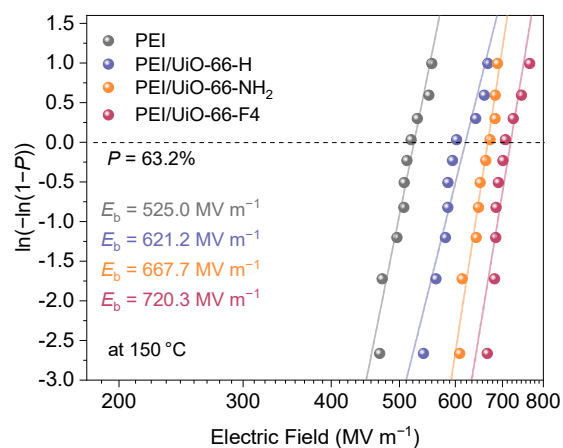
Fig. S20 Weibull breakdown statistics of PEI, PEI/UiO-66-H, PEI/UiO-66-NH$_2$ and PEI/UiO-66-F4 composite films at 1 wt% filler loading at 150 °C.

Table S4 Weibull breakdown parameters of PEI, PEI/UiO-66-H, PEI/UiO-66-NH$_2$ and PEI/UiO-66-F4 composite films at 1 wt% filler loading at 150 °C and 200 °C.

	PEI		**PEI/UiO-66-H**		**PEI/UiO-66-NH$_2$**		**PEI/UiO-66-F4**	
	E_b (MV m^{-1})	β	E_b (MV m^{-1})	β	E_b (MV m^{-1})	β	E_b (MV m^{-1})	β
150 °C	525.0	20.5	621.2	16.0	667.7	30.6	720.3	22.9
200 °C	443.5	9.0	589.2	15.6	626.6	22.9	680.8	27.0
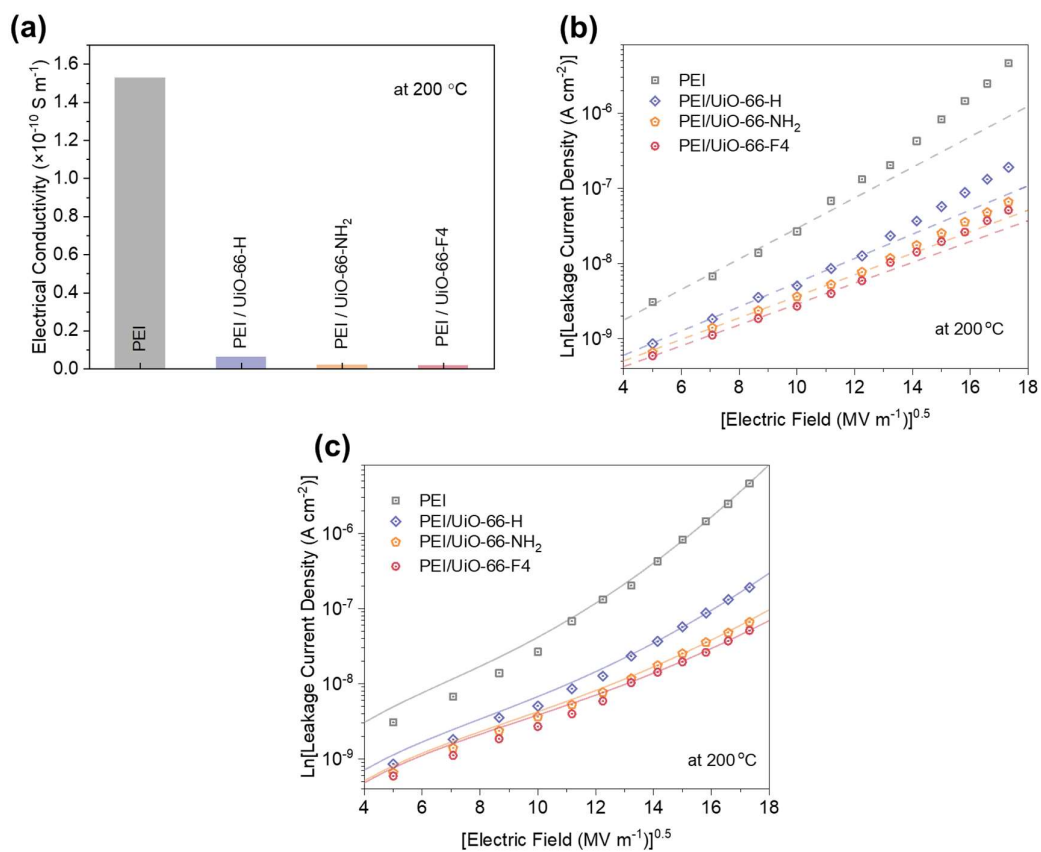
Fig. S21 (a) Electrical conductivity, (b) Linear fitting (dotted lines represent linear fittings) and (c) Hopping conduction fitting (solid lines represent hopping conduction fittings) from leakage current testing results of PEI, PEI/UiO-66-H, PEI/UiO-66-NH$_2$ and PEI/UiO-66-F4 composite films at 1 wt% filler loading at 200 °C.
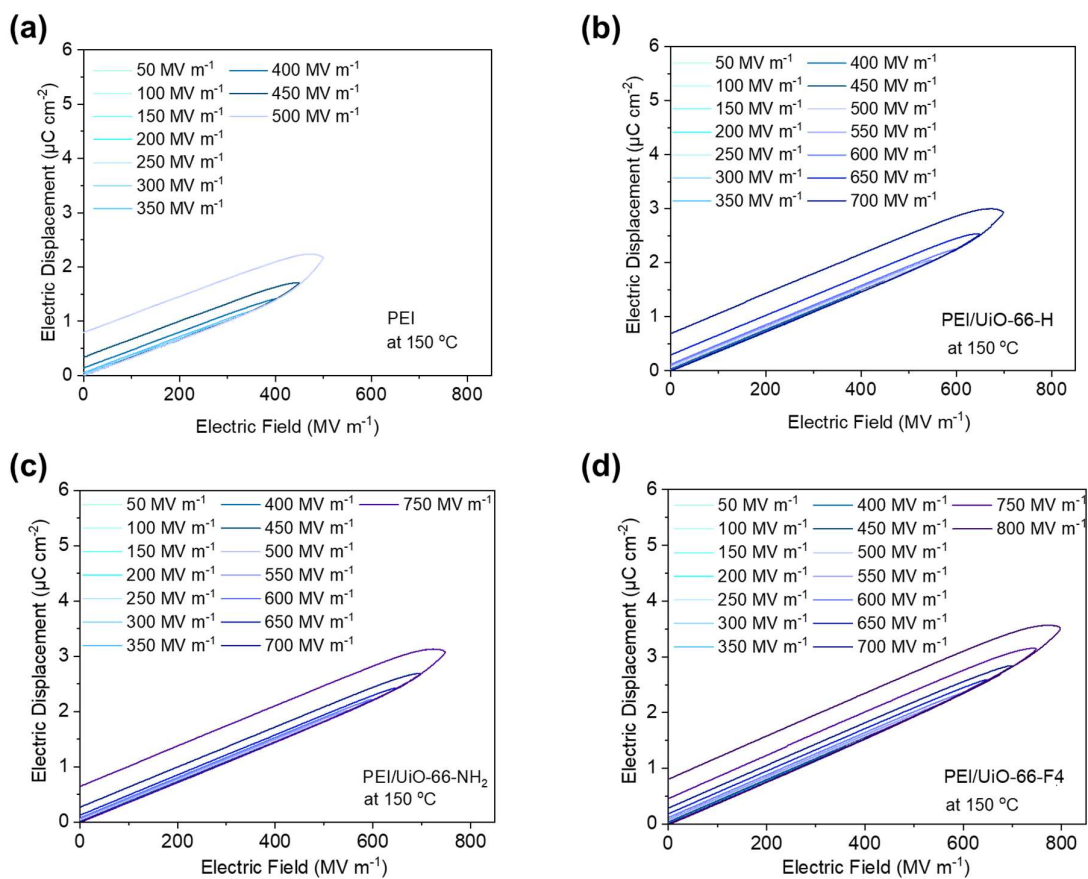
**Fig. S22** *D-E* curves under different electric fields of (a) PEI, (b) PEI/UiO-66-H, (c) PEI/UiO-66-NH$_2$ and (d) PEI/UiO-66-F4 composite films at 1 wt% filler loading at 150 °C.
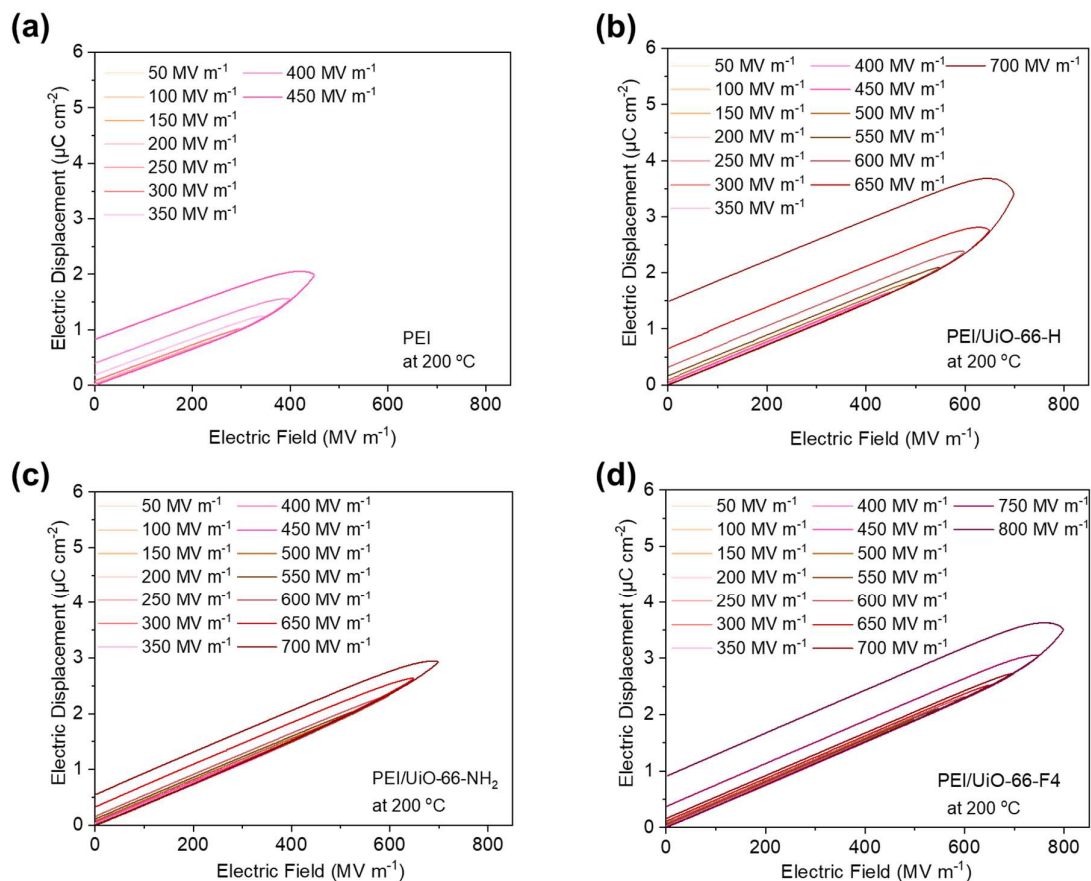
Fig. S23 *D-E* curves under different electric fields of (a) PEI, (b) PEI/UiO-66-H, (c) PEI/UiO-66-NH₂ and (d) PEI/UiO-66-F4 composite films at 1 wt% filler loading at 200 °C.
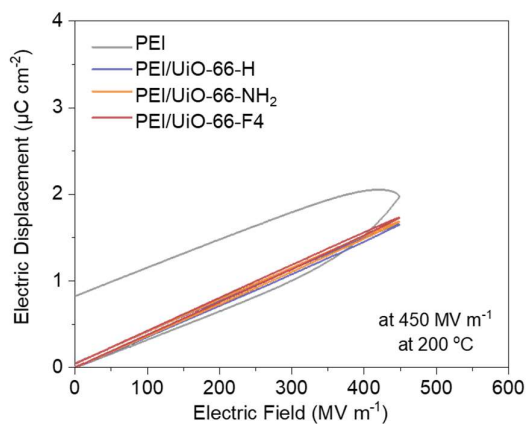
Fig. S24 Comparison of *D-E* curves of PEI, PEI/UiO-66-H, PEI/UiO-66-NH₂ and PEI/UiO-66-F4 composite films at 1 wt% filler loading at 450 MV m⁻¹ and 200 °C.
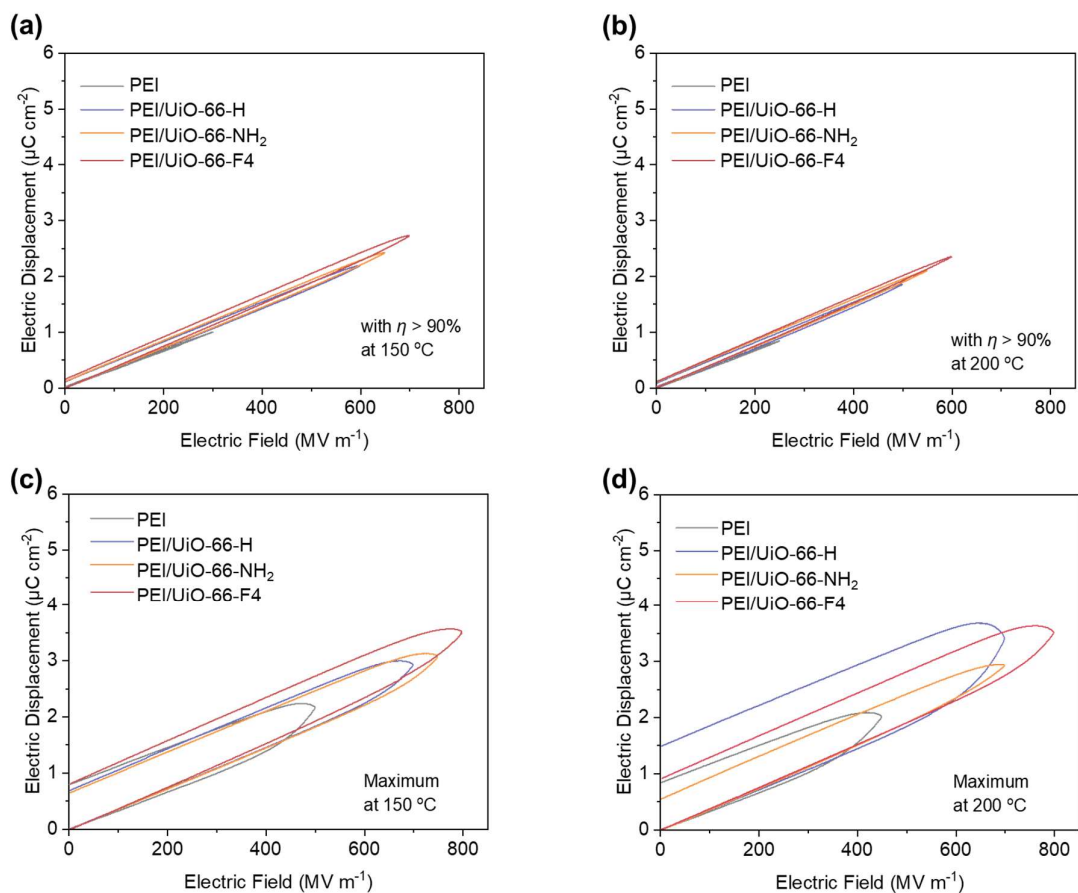
Fig. S25 Comparison of *D-E* curves at $\eta > 90\%$ of PEI, PEI/UiO-66-H, PEI/UiO-66-NH$_2$ and PEI/UiO-66-F4 composite films at 1 wt% filler loading at (a) 150 °C and (b) 200 °C. Comparison of *D–E* curve at maximum U_d of PEI, PEI/UiO-66-H, PEI/UiO-66-NH$_2$ and PEI/UiO-66-F4 composite films at 1 wt% filler loading at (c) 150 °C and (d) 200 °C.
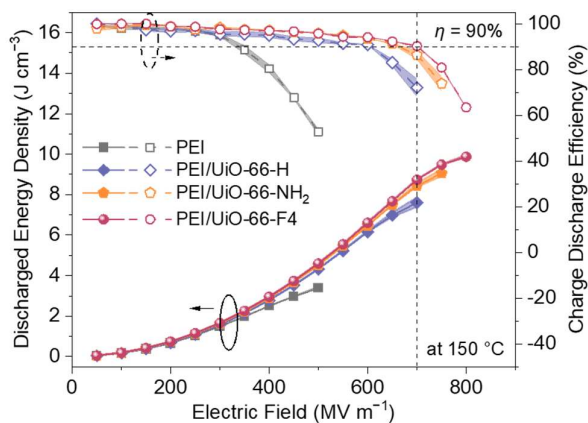
Fig. S26 Comparison of U_d and η of PEI, PEI/UiO-66-H, PEI/UiO-66-NH$_2$ and PEI/UiO-66-F4 composite films at 1 wt% filler loading at 150 °C.

21
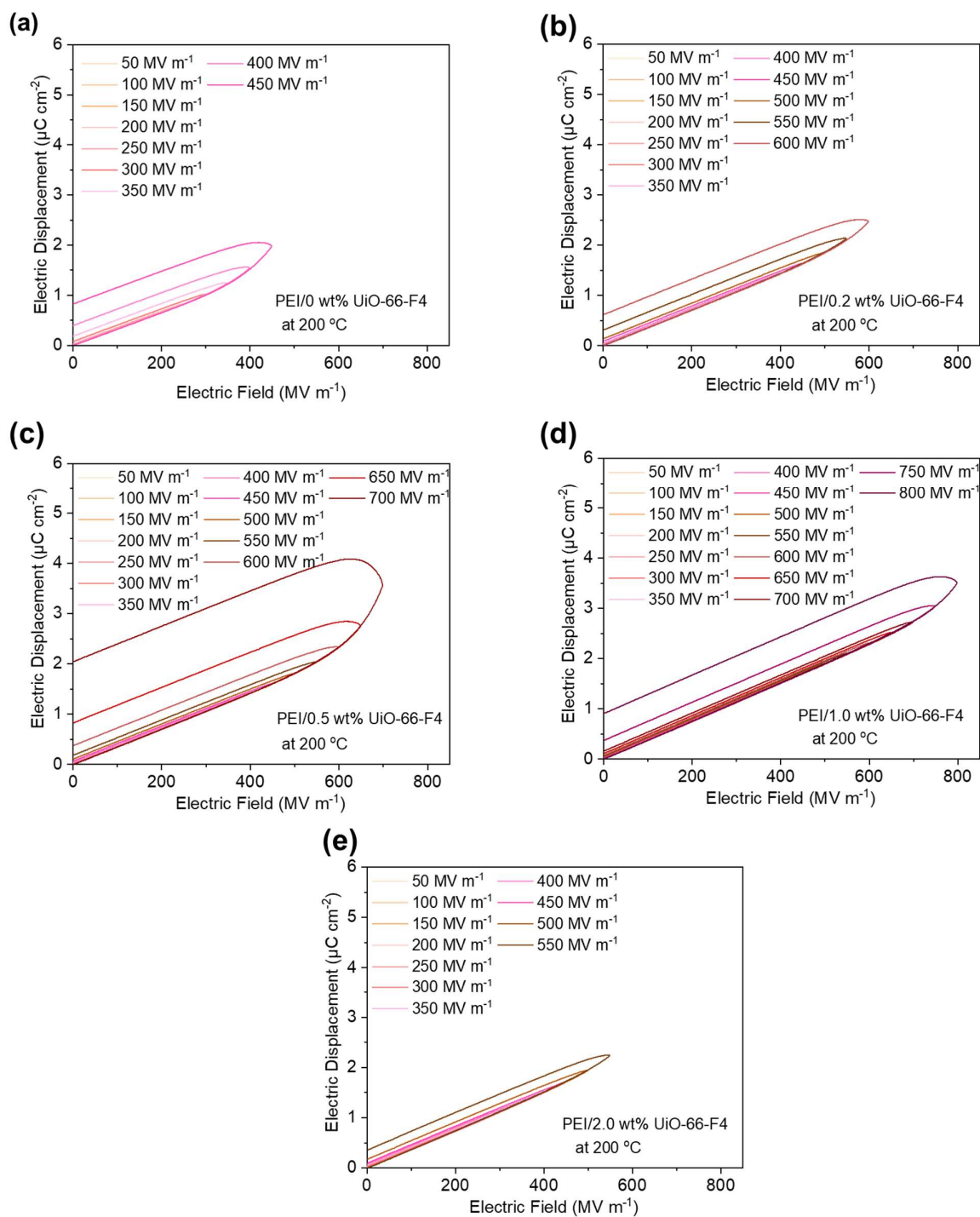
Fig. S27 *D–E* curves under different electric fields of PEI/UiO-66-F4 composite films at different loading ratios of (a) 0 wt%, (b) 0.2 wt%, (c) 0.5 wt% (d) 1.0 wt% and (e) 2.0 wt% at 200 °C.
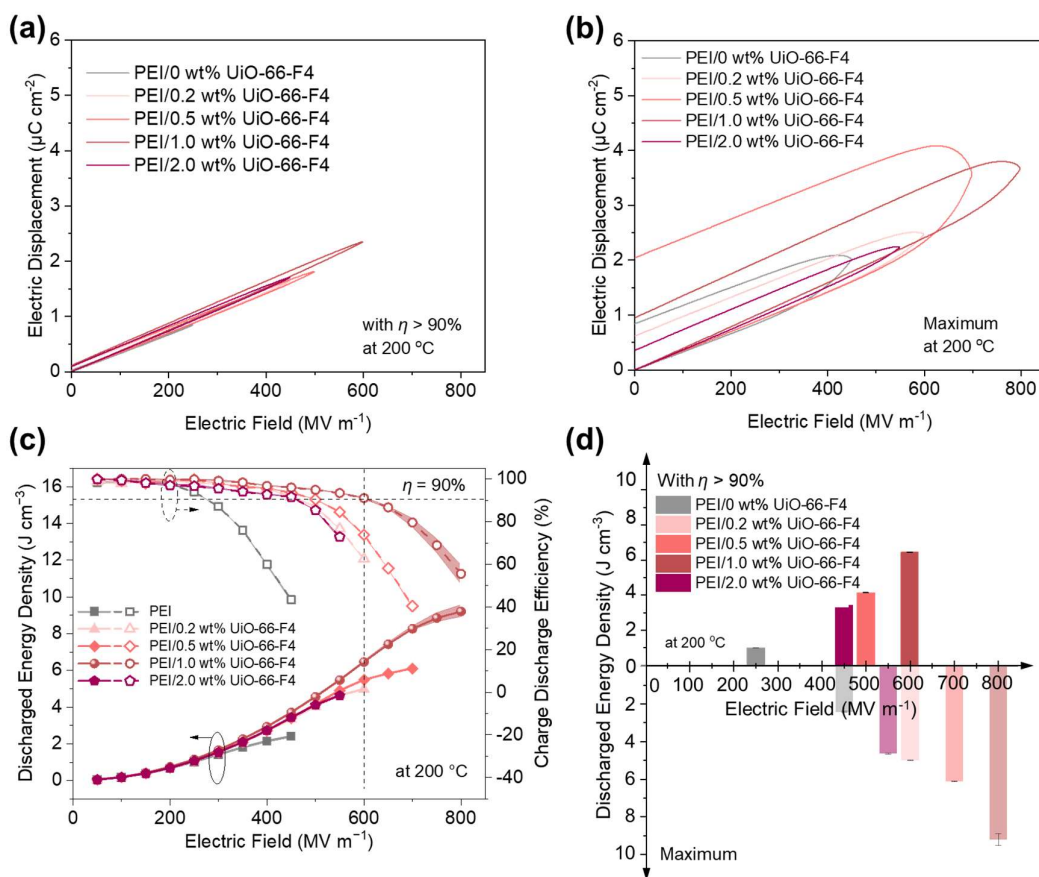
Fig. S28 (a) Comparison of *D–E* curves at $\eta > 90\%$, (b) comparison of *D–E* curves at maximum U_d, (c) Comparison of U_d, η, and (d) comparison of maximum U_d and U_d at $\eta > 90\%$ of PEI/UiO-66-F4 composite films at different loading ratios of 0 wt%, 0.2 wt%, 0.5 wt% 1.0 wt% and 2.0 wt% at 200 °C.

Table S5 Comparison of energy storage performance of PEI/UiO-66-F4 composite films with different loading ratios at 200 °C.

Loading Ratios	Maximum U_d (J cm^{-3})	U_d with $\eta > 90\%$ (J cm^{-3})
0 wt%	2.40	1.01
0.2 wt%	4.98	3.34
0.5 wt%	6.10	4.15
1.0 wt%	9.21	6.45
2.0 wt%	4.63	3.43
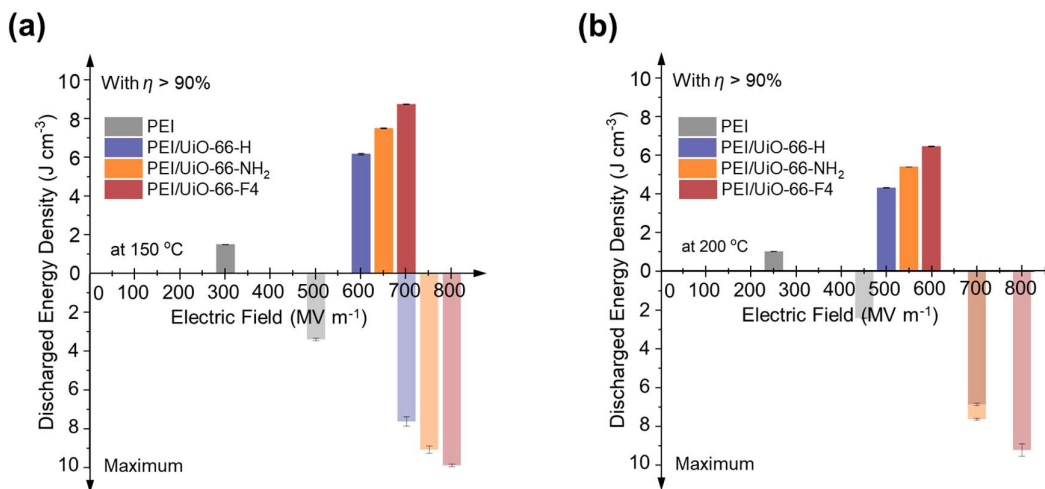
Fig. S29 Comparison of maximum U_d and U_d at $\eta > 90\%$ of PEI, PEI/UiO-66-H, PEI/UiO-66-NH$_2$ and PEI/UiO-66-F4 composite films at 1 wt% filler loading at (a) 150 °C and (b) 200 °C.

**Table S6** Comparison of energy storage performance among lab-synthesized polymers at 150 °C and 200 °C.

Dielectric materials	150 °C		200 °C		Ref.
	Applied field ($MV\ m^{-1}$)	Maximum U_d ($J\ cm^{-3}$)	Applied field ($MV\ m^{-1}$)	Maximum U_d ($J\ cm^{-3}$)	
SO-PI-14.3	/	/	500	4.5	*Adv. Energy Mater.*, 2024, **14**, 2303732.
sc-PEENA	550	5.5	500	4.5	*Angew. Chem. Int. Ed.*, 2024, **63**, e202319766.
p-POClNB	800	8.3	800	7.2	*Adv. Mater.*, 2024, 36, 2402133.
PSBNP-*co*-PTNI$_{0.02}$	760	10.5	720	8.5	*Nature*, 2023, **615**, 62.
CS-ODA	650	7.0	/	/	*Adv. Mater.*, 2023, **35**, 2207580.
PI-spiro-2-5	750	8.2	700	6.2	*Adv. Mater.*, 2023, **35**, 2303849.
Polysulfate P3	600	6.0	/	/	*Joule*, 2023, **7**, 95.
PEI-iso	700	7.5	/	/	*Nat. Commun.*, 2023, **14**, 2406.
PI-oxo-iso	700	7.0	700	6.2	
o-POFNB	800	8.5	700	6.5	*Energy Environ. Sci.*, 2022, **15**, 1307.
m-POFNB	700	7.4	/	/	*Proc. Nat. Acad. Sci.*, 2021, **118**, 2115367118.
POFNB	680	5.7	/	/	*Adv. Mater.*, 2020, **32**, 2000499.
PEI/ UiO-66-F4	**800**	**9.87**	**800**	**9.21**	**This Work**

Table S7 Comparison of energy storage performance among polymer composites at 150 ℃ and 200 ℃.

Dielectric materials	150 ℃		200 ℃		Ref.
	Applied field (MV m^{-1})	Maximum U_d (J cm^{-3})	Applied field (MV m^{-1})	Maximum U_d (J cm^{-3})	
F-PI-PWNS	900	10.5	820	8.8	*Nat. Energy*, 2024, **9**, 143.
PEI-PWNS	700	7.8	660	6.6	
CNO@MOF/PI	660	5.5	/	/	*Adv. Mater.*, 2024, **36**, 2402239.
H-Al$_2$O$_3$/PEI	660	6.6	560	4.7	*Energy Environ. Sci.*, 2024, **17**, 1592.
PEI/ZrO$_2$@COF	600	6.2	/	/	*Adv. Funct. Mater.*, 2024, **34**, 2314910.
FPI-TE	850	10.0	720	6.5	*Adv. Mater.*, 2023, **35**, 2302392.
PEI-TE	700	6.2	640	5.8	
PEN-DCPD/F-TCNQ$_{0.2}$	750	9.6	/	/	*Adv. Mater.*, 2023, **35**, 2306562.
PI-3.0	600	5.6	550	4.3	*Adv. Mater.*, 2023, **35**, 2211487.
PEI-OH/Al$_2$O$_3$-NP	/	/	650	6.8	*Adv. Mater.*, 2023, **35**, 2301936.
PEI/HEnf	580	6.5	/	/	*Adv. Energy Mater.*, 2023, **13**, 2203925 .
PC/ITIC	650	6.8	/	/	*Adv. Energy Mater.*, 2023, **13**, 2203961.
FPE/ITIC	/	/	600	5.5	
F-PI/PCBM	709	6.39	580	4.6	*Adv. Mater.*, 2022, **34**, 2207421.
PEI/Al$_2$O$_3$@ZrO$_2$	520	5.2	/	/	*Adv. Energy Mater.*, 2021, **11**, 2101297.
TiO$_2$-PEI/BNNS-PEI	500	4.6	/	/	*Adv. Mater.*, 2021, **33**, 2103338.
PEI/PCBM	550	4.8	450	3.2	*Nat. Commun.*, 2020, **11**, 3919.
PEI/UiO-66-F4	**800**	**9.87**	**800**	**9.21**	**This Work**
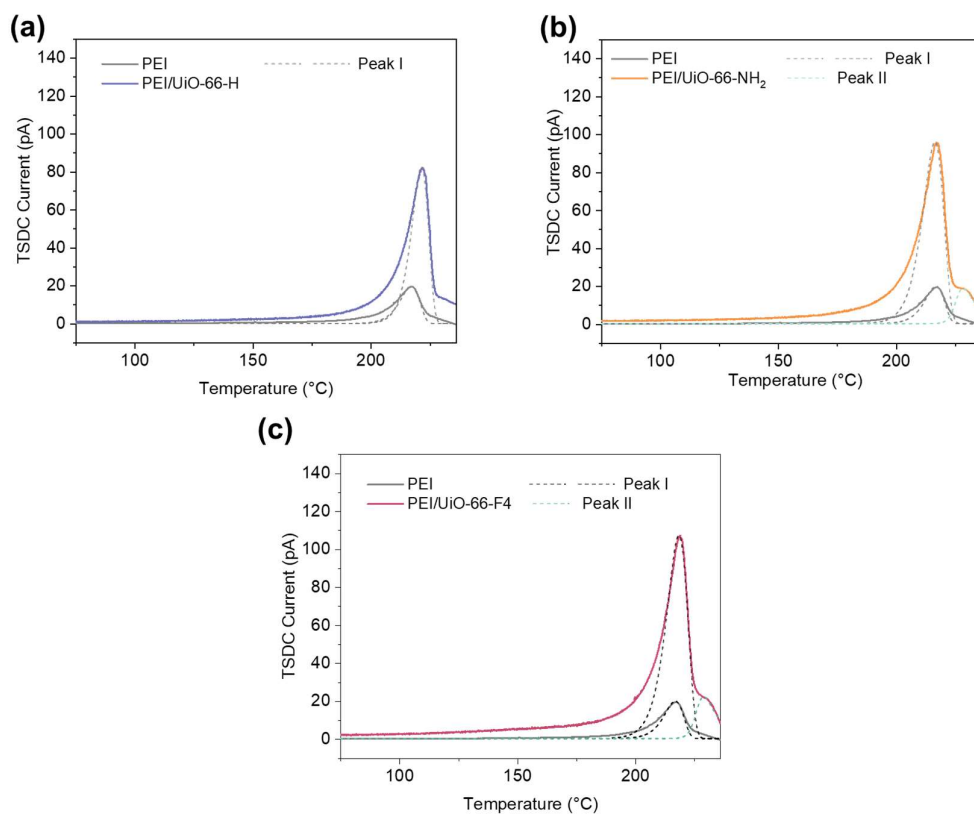
Fig. S30 Comparison of thermally stimulated depolarization current (TSDC) curves between PEI and (a) PEI/UiO-66-H, (b) PEI/UiO-66-NH$_2$ and (c) PEI/UiO-66-F4 composite films at 1 wt% filler loading. The solid lines are experimental results while the short-dashed lines are from peak fitting.
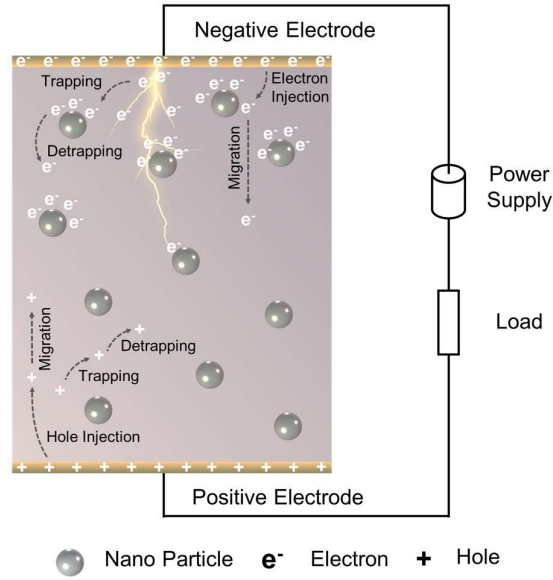
Fig. S31 Scheme of the established two-dimensional bipolar carrier transport-dielectric breakdown (2D BCT-DB) model, in which purple square represents the polymer matrix, and gray balls represent MOF nanoparticles.

Note S1: **Space Charge Simulation**

The bipolar carrier transport model concerns the main processes such as charge injection, migration, trapping and de-trapping, recombination and extraction.

Charge transport can be described by the current continuity equation, the Poisson equation and the transport equation as follows: [S1]

$$
\begin{cases}
\dfrac{\partial n_a(x,t)}{\partial t} + \dfrac{\partial f_a(x,t)}{\partial x} = S_a(x,t) \\[2ex]
\dfrac{\partial E(x,t)}{\partial x} = \dfrac{\rho_{all}(x,t)}{\varepsilon_0 \varepsilon_r} \\[2ex]
f_a(x,t) = \mu_a(x,t) n_a(x,t) E(x,t) - e D_f \dfrac{\mathrm{d}n}{\mathrm{d}x}
\end{cases}
\qquad \text{(Equation S1)}
$$

where subscript a represents the types of carriers, including free electrons ($e\mu$), free holes ($h\mu$), trapped electrons (et) and trapped holes (ht); n_a is the carrier concentration, $C \cdot m^{-3}$; f_a is the carrier flux density, $A \cdot m^{-2}$; t is the time, s; x is the coordinate, m; ρ_{all} is the total charge density, $C \cdot m^{-3}$; μ_a is the mobility of carriers, $m^2 \cdot V^{-1} \cdot s^{-1}$; D_f is the diffusion coefficients, $m^2 \cdot s^{-1}$.

The specific expression describing the processes of trapping, de-trapping and recombination of different types of carriers is as follows: [S2]

$$
\begin{cases}
S_{\text{e}\mu} = -S_1 \cdot n_{\text{e}\mu} \cdot n_{\text{ht}} - S_3 \cdot n_{\text{e}\mu} \cdot n_{\text{h}\mu} - B_{\text{e}} \cdot n_{\text{e}\mu} \cdot (1 - \dfrac{n_{\text{et}}}{N_{\text{eto}}}) + D_{\text{e}} \cdot n_{\text{et}} \\[2mm]
S_{\text{et}} = -S_2 \cdot n_{\text{et}} \cdot n_{\text{h}\mu} - S_0 \cdot n_{\text{et}} \cdot n_{\text{ht}} + B_{\text{e}} \cdot n_{\text{e}\mu} \cdot (1 - \dfrac{n_{\text{et}}}{N_{\text{eto}}}) - D_{\text{e}} \cdot n_{\text{et}} \\[2mm]
S_{\text{h}\mu} = -S_2 \cdot n_{\text{et}} \cdot n_{\text{h}\mu} - S_3 \cdot n_{\text{e}\mu} \cdot n_{\text{h}\mu} - B_{\text{h}} \cdot n_{\text{h}\mu} \cdot (1 - \dfrac{n_{\text{ht}}}{N_{\text{hto}}}) + D_{\text{h}} \cdot n_{\text{ht}} \\[2mm]
S_{\text{ht}} = -S_1 \cdot n_{\text{et}} \cdot n_{\text{h}\mu} - S_0 \cdot n_{\text{et}} \cdot n_{\text{ht}} + B_{\text{h}} \cdot n_{\text{h}\mu} \cdot (1 - \dfrac{n_{\text{ht}}}{N_{\text{hto}}}) - D_{\text{h}} \cdot n_{\text{ht}}
\end{cases}
\qquad \text{(Equation S2)}
$$

where S_0 is the recombination coefficient of trapped electron and trapped hole, $\text{m}^3 \cdot \text{C}^{-1} \cdot \text{s}^{-1}$; S_1 is the recombination coefficient of free electron and trapped hole, $\text{m}^3 \cdot \text{C}^{-1} \cdot \text{s}^{-1}$; S_2 is the recombination coefficient of trapped electron and free hole, $\text{m}^3 \cdot \text{C}^{-1} \cdot \text{s}^{-1}$; S_3 is the recombination coefficient of free electron and free hole, $\text{m}^3 \cdot \text{C}^{-1} \cdot \text{s}^{-1}$; B_{e} and B_{h} are the trapping coefficients of electron and hole traps, respectively, s^{-1}; N_{eto} and N_{hto} are the concentrations of electron traps and hole traps, respectively, $\text{C} \cdot \text{m}^{-3}$; D_{e} and D_{h} are the de-trapping coefficients of electron and hole, respectively, s^{-1}.

The charge injection from electrodes is typically described by the Schottky law as follows: [S2]

$$
\begin{cases}
j_{\text{ei}}(0,t) = AT^2 \exp(\dfrac{-e\omega_{\text{ei}}}{kT}) \exp(\dfrac{e}{kT}\sqrt{\dfrac{e|E(0,t)|}{4\pi\varepsilon_0\varepsilon_{\text{r}}}}) \\[4mm]
j_{\text{hi}}(D,t) = AT^2 \exp(\dfrac{-e\omega_{\text{hi}}}{kT}) \exp(\dfrac{e}{kT}\sqrt{\dfrac{e|E(D,t)|}{4\pi\varepsilon_0\varepsilon_{\text{r}}}})
\end{cases}
\qquad \text{(Equation S3)}
$$

where $j_{\text{ei}}(0,t)$ and $j_{\text{hi}}(D,t)$ are the injection current densities at cathode ($x=0$) and anode ($x=D$), respectively, $\text{A} \cdot \text{m}^{-2}$; ω_{hi} and ω_{ei} are the Schottky injection barriers for holes and electrons, respectively, eV; $A=1.2\times10^6$ $\text{A} \cdot \text{m}^{-1} \cdot \text{K}^{-2}$, is the Richardson constant; $k=1.38\times10^{-23}$ $\text{J} \cdot \text{K}^{-1}$, is the Boltzmann constant.

During the transport process, hopping conduction between carriers in shallow traps is considered as follows:

$$
\mu(x,t) = \frac{2v\lambda}{E(x,t)} \exp(\frac{-e\omega_\mu}{kT}) \sinh(\frac{eE(x,t)\lambda}{2kT})
\qquad \text{(Equation S4)}
$$

where $\mu(x,t)$ is the carrier mobility considering hopping conduction, $\text{m}^2 \cdot \text{V}^{-1} \cdot \text{s}^{-1}$; λ is the hopping distance, nm; ω_μ is the hopping barrier height, eV; v is the attempt-to-escape frequency, which is set to 6.7×10^{12} Hz. [S3]

The free charges can be trapped in deep traps with the trapping coefficients, which are described as follows: [S4,S5]

$$
B = \frac{\mu_{\text{a}} \cdot N_{\text{t}} \cdot e}{\varepsilon_0 \cdot \varepsilon_r}
\qquad \text{(Equation S5)}
$$

where μ_a is the mobility of charges, $m^2 \cdot V^{-1} \cdot s^{-1}$; N_t is the trap density, m^{-3}; $e=1.6 \times 10^{-19}$ C, is the electronic charge.

Trapped charges can escape from deep traps by overcoming a potential barrier and the de-trapping coefficient is as follows: [S6]

$$D = \nu \cdot \exp(\frac{-\Delta Utr}{k_B T}) \qquad \text{(Equation S6)}$$

where ΔU_{tr} is the de-trapping barrier, eV, which is obtained from TSDC results.

The extraction of carriers at the electrode is assumed to be as normal conduction process with an extraction barrier as follows: [S6]

$$j_{e,h}(x,t) = n_{e\mu,h\mu} \mu_{e,h} E(x,t) \qquad \text{(Equation S7)}$$

where j_e and j_h are the extraction current density of electrons and holes, respectively, $A \cdot m^{-2}$; $n_{e\mu}$ and $n_{h\mu}$ are the charge density of mobile electrons and holes, respectively; μ_e and μ_h are the mobilities of electrons and holes, respectively.

The PEI polymer matrix is set as a cuboid with length=l, width=d and height=h and particle is set as a sphere with radius=r in the 2-D model. The density of particle and PEI are $\rho_{particle}$ and ρ_{PEI}, respectively. The doping ratio of PEI composites is z in mass fraction. The number of doped particles can be calculated as follows:[S7]

$$N_{particle} = \frac{3}{2} \cdot \frac{ld}{1+(\frac{1}{z}-1) \cdot \dfrac{\rho_{Particle}}{\rho_{PEI}}} \cdot \frac{1}{\pi r^2} \qquad \text{(Equation S8)}$$

The relative dielectric constant of the interface zone between doped particles and the PEI matrix is calculated as 5.3 for simulation as follows :[S7]

$$\chi_{interface}^{optimal} \approx 2 \times \chi_{matrix} \qquad \text{(Equation S9)}$$

$$k \approx 1 + \chi \qquad \text{(Equation S10)}$$

where χ is the dielectric susceptibility; k is the relative dielectric constant; $\chi_{interface}^{optimal}$ is the optimal dielectric susceptibility of the interface zone; and χ_{matrix} is the dielectric susceptibility of the matrix.

Model 0 represents the filler-free PEI samples, with the square of 10 μm × 10 μm. The simulation parameters are shown in Table S8. Model 1 represents PEI/UiO-66-NH$_2$ composites. The thickness of the interface zone between polymer and MOF is set to be 20 nm. The free charges would be blocked by the injection barrier (1 eV) at the interface zone in Model 1. The Model 2 represents PEI/UiO-66-F4 composites. The thickness of the interface zone is 20 nm, and free charges would be captured by deep traps of the interface zone in Model 2. Therefore, the trapping coefficients and deep trap depth in Model 1 are different from Model 0 and Model 2, which are shown in Table S9.

**Table S8** Parameters in the two-dimensional model.

	l	d	r	z	$N_{particle}$
PEI/UiO-66-NH₂	10 μm	10 μm	40 nm	1%	378
PEI/UiO-66-F4	10 μm	10 μm	40 nm	1%	378

Table S9 Parameters for bipolar carrier transport model simulation.

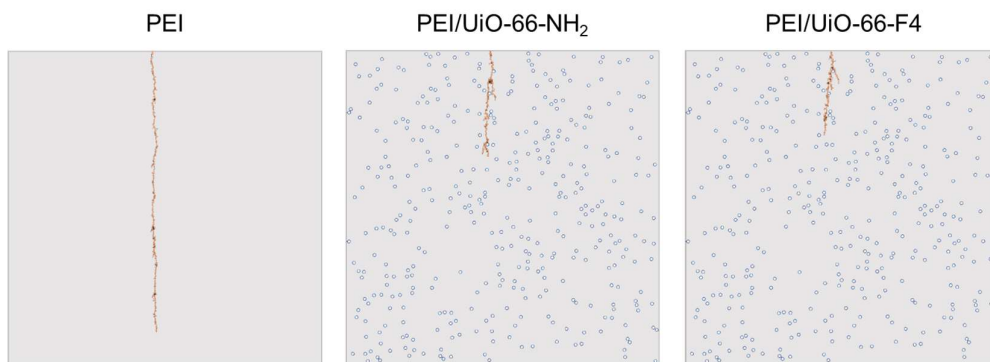|	Parameter	PEI	PEI/UiO-66-NH₂	PEI/UiO-66-F4
Injection	Injection barrier for matrix	2.2 eV	2.2 eV	2.2 eV
	Injection barrier for interface zone	/	2 eV	/
Transport	Hopping barrier height in matrix	1.57 eV	1.57 eV	1.57 eV
	Hopping distance in matrix	1.92 nm	1.92 nm	1.92 nm
	Hopping barrier height at the interface zone	/	1.52 eV	1.52 eV
	Hopping distance in the interface zone	/	1.11 nm	1.02 nm
	Trapping coefficient in the matrix	$0.07\ \mathrm{s}^{-1}$	$0.07\ \mathrm{s}^{-1}$	$0.07\ \mathrm{s}^{-1}$
Trapping & De-trapping	Deep trap depth	1.75 eV	1.75 eV	1.75 eV
	Trapping coefficient at the interface zone	/	$0.1\ \mathrm{s}^{-1}$	$0.1\ \mathrm{s}^{-1}$
	Deep trap depth at the interface zone	/	1.75 eV	2.00 eV
Recombination	S_0, S_1, S_2	5×10^3	5×10^3	5×10^3
Basic	Electric field E	$400\ \mathrm{MV \cdot m^{-1}}$	$400\ \mathrm{MV \cdot m^{-1}}$	$400\ \mathrm{MV \cdot m^{-1}}$
	Temperature T	200 ℃	200 ℃	200 ℃
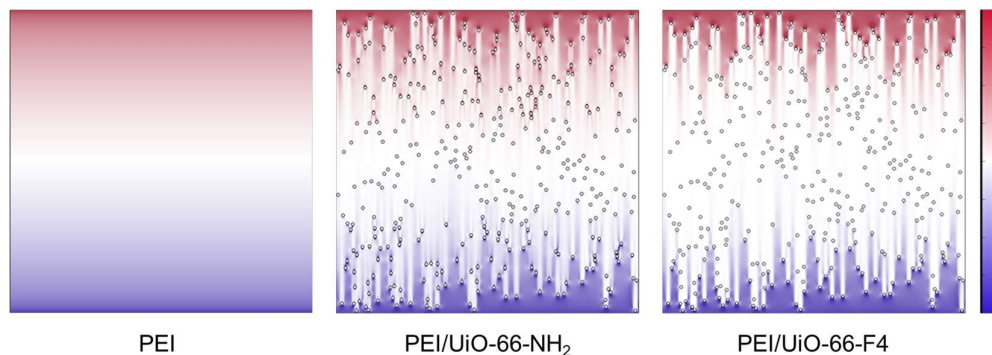
Fig. S32 Simulated space charge density distribution of PEI, PEI/UiO-66-NH$_2$ and PEI/UiO-66-F4 composite at 1 wt% filler loading at 200 °C and 400 MV m^{-1}.
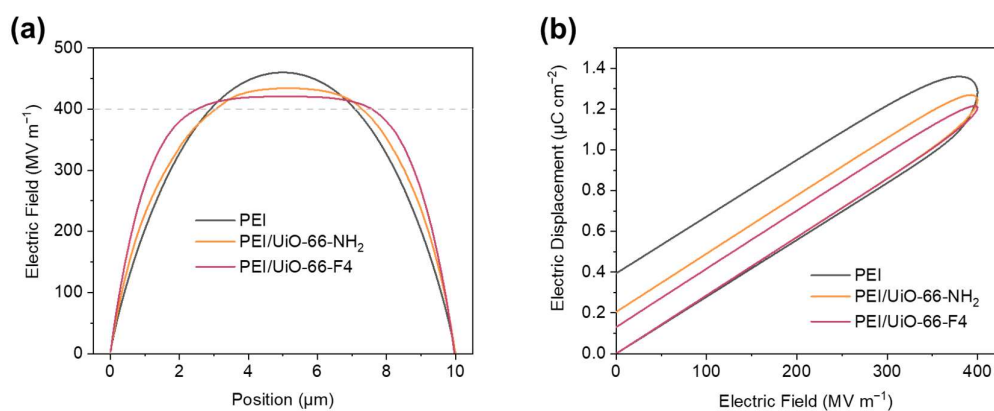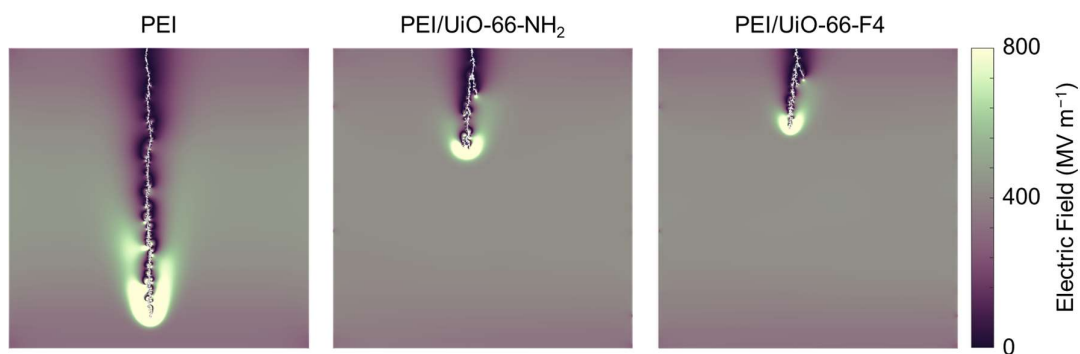

Fig. S33 Simulated (a) electric field distribution and (b) *D–E* loop of PEI, PEI/UiO-66-NH$_2$ and PEI/UiO-66-F4 composite at 1 wt% filler loading at 200 °C and 400 MV m^{-1}.
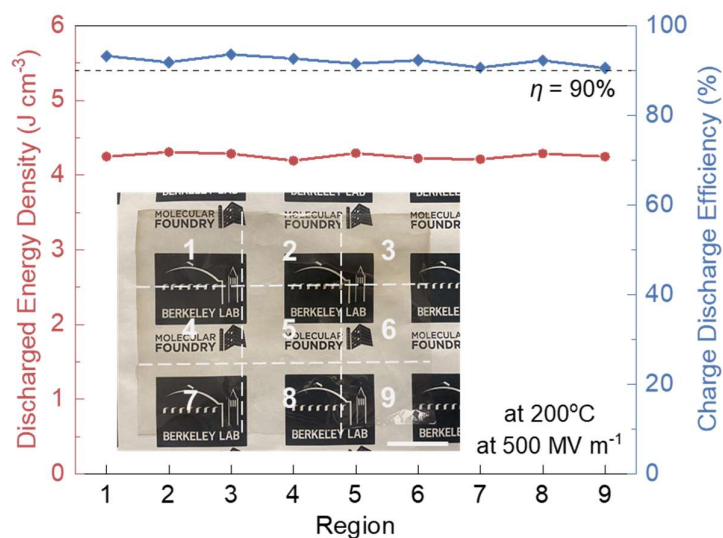
Fig. S34 Simulated electric tree propagation of PEI, PEI/UiO-66-NH$_2$ and PEI/UiO-66-F4 composites at 1 wt% filler loading at 200 °C and 400 MV m^{-1}.

Fig. S35 Simulated electric field distribution after electric tree propagation of PEI, PEI/UiO-66-NH$_2$ and PEI/UiO-66-F4 composites at 1 wt% filler loading at 200 °C and 400 MV m^{-1}.

Fig. S36 Discharged energy storage characteristics of devices fabricated on nine different regions of a large-area PEI/ UiO-66-F4 film at 1 wt% filler loading measured at 200 °C and 500 MV m^{-1}. Inset: pictures of a roll of the composite film, and 9 devices areas marked on one film. The scale bar is 3 cm.
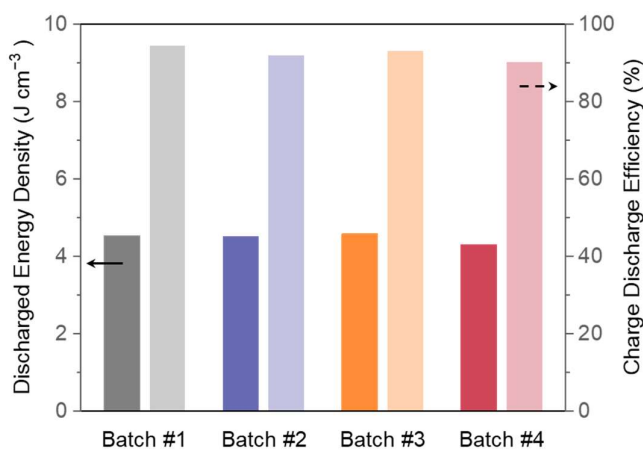
Fig. S37 Discharged energy storage characteristics of different batches of PEI/UiO-66-F4 composite films, all at 1 wt% filler loading and measured at 200 °C and 500 MV m^{-1}. Respective date of measurement: batch #1 08/15/2023, #2 09/05/2023, #3 12/11/2023, #4 02/23/2024.

The interquartile range (IQR) is the range of values that resides in the middle of all measured results (in this case, energy storage performance including U_d and η). Quartiles are the partitioned values that divide the whole values into four equal parts, and IQR defines the difference between the third and the first quartile, as follows:

$$IQR = Q_3 - Q_1 \hspace{3cm} \text{(Equation S11)}$$

where Q_1 is the lower quartile, and Q_3 is the upper quartile.

For a normal distribution of measuring results, other than the mean value, the median value is always used to better evaluate the effective value. With the appropriate measure of variability, the median is the middle value of IQR.
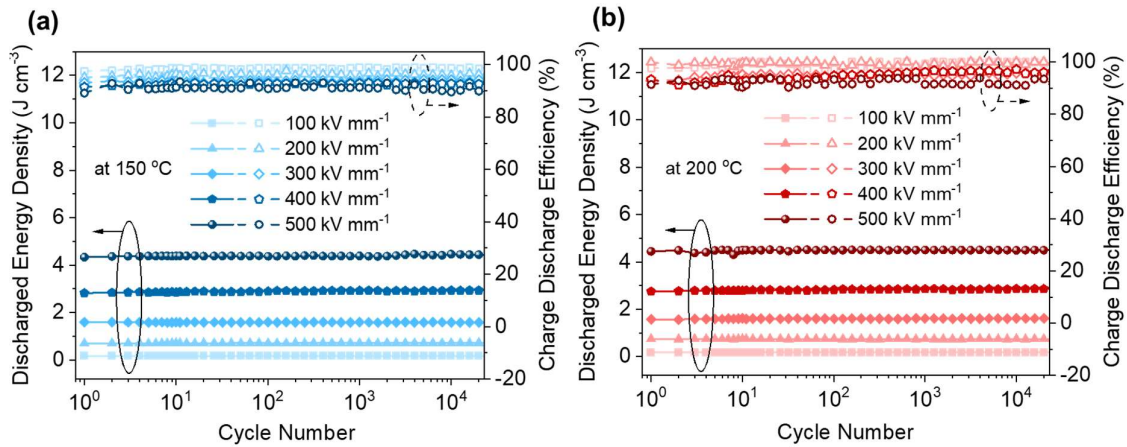
Fig. S38 Cyclic stability of devices based on PEI/UiO-66-F4 composite at 1 wt% filler loading, measured at (a) 150 °C and (b) 200 °C, at different electric fields of 100 MV m^{-1}, 200 MV m^{-1}, 300 MV m^{-1}, 400 MV m^{-1} and 500 MV m^{-1}.

Table S10 Cost estimate of PEI/MOF composites at 1 wt% filler loading. The cost of polyetherimide (PEI) pellet is based on current prices ($300/500 g) from PolyK Technologies; the costs of ligands (Terephthalic acid: $72.9/1 kg, 2-Aminoterephthalic acid: $111/25 g, Tetrafluoroterephthalic acid: $219/5 g), metal ions (ZrCl$_4$: $1520/5 kg), modulators (Formic acid: $559/4 L, Benzoic acid: $483/3 kg, HCl: $475/12 L) and solvents (DMF: $3020/200 L, THF: $1161/18 L, NMP: $1810/18 L) are based on current prices from Sigma-Aldrich. The costs may vary significantly from vendor to vendor. The total costs of MOFs are calculated based on 1 mol scale with the unit price in $/g. The total costs of PEI composites are calculated with the unit price in $/100 g at 1 wt% filler loading.

	Ligands	Metal Ion	Modulators	Solvents	Products
Material	Terephthalic acid	ZrCl$_4$	Formic acid	DMF	**UiO-66-H**
Amount	0.996 kg	1.398 kg	19.320 kg	72.000 L	1.660 kg
Total Cost	$ 72.61	$ 424.99	$ 2213.09	$ 1087.20	$ 3797.89
Unit Cost	\	\	\	\	**$ 2.29/g**
Material	2-Aminoterephthalic acid	ZrCl$_4$	Benzoic acid	DMF	**UiO-66-NH$_2$**
Amount	1.086 kg	1.398 kg	21.960 kg	72.000 L	1.754 kg
Total Cost	$ 4821.84	$ 425.60	$ 3535.56	$ 1087.20	$ 9870.2
Unit Cost	\	\	\	\	**$ 5.63/g**
Material	Tetrafluoroterephthalic acid	ZrCl$_4$	HCl	THF	**UiO-66-F$_4$**
Amount	1.428 kg	1.398 kg	2.160 kg	72.000 L	2.092 kg
Total Cost	$ 62546.40	$ 425.60	$ 57.38	$ 4644.00	$ 67673.38
Unit Cost	\	\	\	\	**$ 32.35/g**
Material	\	\	\	NMP	**PEI**
Amount	\	\	\	2.5 L	100 g
Total Cost	\	\	\	$ 251.39	$ 60
Unit Cost	\	\	\	\	**$ 331.39/100 g**
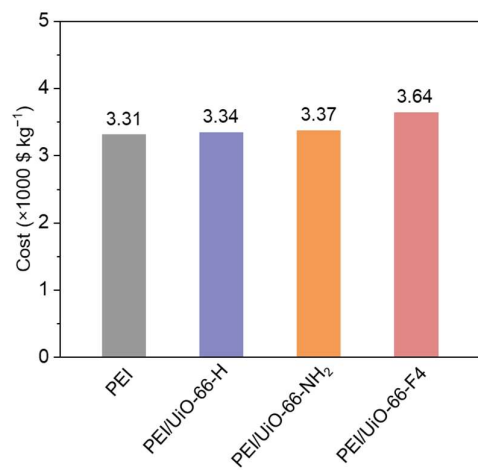
Fig. S39 Cost comparison of PEI/MOF composites at 1 wt% filler loading.

References

S1. Z. Lv, X. Wang, K. Wu, X. Chen, Y. Cheng and L. A. Dissado, *IEEE Trans. Dielectr. Electr. Insul.*, 2013, **20**, 337.

S2. S. Le Roy, P. Segur, G. Teyssedre and C. Laurent, *J. Phys. D: Appl. Phys.*, 2004, **37**, 298.

S3. H. Eyring, *J. Chem. Phys.*, 1935, **3**, 107.

S4. M. Kuik, L. J. A. Koster, G. A. H. Wetzelaer and P. W. M. Blom, *Phys. Rev. Lett.*, 2011, **107**, 256805.

S5. M. Kuik, L. J. A. Koster, A. G. Dijkstra, G. A. H. Wetzelaer and P. W. M. Blom, *Org. Electron.*, 2012, **13**, 969.

S6. F. Boufayed, G. Teyssèdre, C. Laurent, S. L. Roy, L. A. Dissado, P. Ségur and G. C. Montanari, *J. Appl. Phys.*, 2006, **100**, 104105.

S7. P. Liu, X. Pang, Z. Xie, T. Xu, S. Shi, P. Wu, H. Li and Z. Peng, *J. Appl. Phys.*, 2022, **132**, 165501.